Master Thesis

Study of $M1$ Quenching in ^{28}Si by a (p, p') Measurement at zero-degrees

Hiroaki MATSUBARA

February, 2006

Department of Physics
Graduate School of Science
Osaka University

Abstract

We have realized ^{28}Si(p,p') measurements with high resolution at forward angles including zero-degrees at $E_p = 295$ MeV at RCNP. The 1^+ ($M1$) excitation has two types of transitions, isoscalar ($T = 0$) and isovector ($T = 1$) ones. The difference between them can give us another aspect of nuclei. A good scattering angle resolution of $0.5-0.8^\circ$ has been achieved by a sieve-slit angle calibration. A good energy resolution of 20 keV in FWHM has been achieved by *dispersion matching technique*. Background events are subtracted reasonably. By comparing the measured angular distribution with distorted wave Born approximation calculation, the isospin value as well as the J^π is assigned for each state. Three states of 1^+, $T = 0$ are newly observed. It can be confirmed that the flatter angular distribution of the 1^+, $T = 0$ state is their common nature. Four states, which were known as 1^+, $T = 0$, are assigned as 0^+ or another natural parity transitions. The measured (p,p') cross sections are extrapolated to $\theta_{cm} = 0^\circ$ and to at zero energy transfer, and are converted to B(σ) strengths. It could be suggested that more strength fragmentations is observed in the isovector excitation than that of isoscalar. The cumulative sums of B(σ) up to $E_x = 16$ MeV are compared with the predictions of recent shell model calculations. Ratios of observed to predicted 1^+ sum are less than unity for both isoscalar and isovector case. The isoscalar ratio is 60 ± 5 % and the isovector one is 76 ± 2 %. Significant differences between the isoscalar and the isovector ratio are not seen. It can be understood that the Δ-hole admixture plays little role in the $M1$ quenching of ^{28}Si.

Abstract

我々はＲＣＮＰにおいて 295MeV に加速された陽子ビームを ^{28}Si のターゲットに照射する実験を行い、０度を含む前方角において超高分解能の陽子非弾性散乱測定に成功した。$M1$ 遷移には $T = 0$ と $T = 1$ の二種類の遷移が存在しており、両者の差異より原子核の新たな情報を得られるであろう。高分解能スペクトロメーターの磁場をアンダーフォーカスモードに設定し、シーブスリットを用いた角度補正を行うことで 0.5 〜 0.8 度の散乱角度分解能を得た。また分散整合法により 20keV の高エネルギー分解能を得、バックグラウンドも美しく除けている。各励起状態のスピンパリティーとアイソスピン励起は、断面積の角度分布を歪曲波ボルン近似（ＤＷＢＡ）計算と比較することにより決定された。高品質データのおかげで３つの新たな $1^+, T = 0$ の準位を観測した。この $1^+, T = 0$ 励起の角度分布は従来考えられていたものよりもずっと平らに近いことがわかり、これは $T = 0$ の遷移機構に共通するものと思われる。また以前に $1^+, T = 1$ と考えられていた励起準位のうちの４つが、実は 0^+ もしくは他のナチュラルパリティの準位であることがわかった。測定で得られた断面積は運動量移行量と励起エネルギーの両者がゼロであるべく値に外挿され、そしてスピンフリップ遷移強度である $\mathrm{B}(\sigma)$ に変換された。$T = 0$ に比べて $T = 1$ での遷移強度のフラグメントが顕著に見られた。励起エネルギーで 16MeV までの遷移強度を足し上げた結果を、シェルモデル計算と比較した。実験値の総和と計算値との比が１よりも小さいという結果が $T = 0$ 励起と $T = 1$ 励起の両方に見られた。得られた比は $T = 0$ 励起で 60 ± 5 %、$T = 1$ 励起で 76 ± 2 %であり、両者に有意の差は見られなかった。以上より ^{28}Si の $M1$ クエンチングに関しては Δ 粒子-空孔の結合がほとんど寄与していないと理解できる。

Contents

1 Introduction **4**

1.1 Quenching problem 4

1.1.1 GT quenching problem 4

1.1.2 $M1$ quenching problem 5

1.2 Isoscalar and isovector transition of $M1$ 6

1.3 Essential points for obtaining conclusive results 7

1.4 Purpose of this work 7

2 Experimental Methods **9**

2.1 Ion source 11

2.1.1 Unpolarized ion source 11

2.1.2 Polarized ion source 11

2.2 Beam Line Polarimeter (BLP) 11

2.3 Target 12

2.4 Magnetic spectrometers 12

2.4.1 Grand Raiden (GR) 12

2.4.2 Large Acceptance Spectrometer (LAS) 14

2.5 Focal plane detector system of GR 16

2.6 Focal plane detector system of LAS 16

2.7 Faraday cup and beam line for the 0° measurement 19

2.8 Beam tuning 21

2.9 Under-focus mode 23

2.9.1 Purpose and principle 23

2.9.2 Sieve-slit Measurement 24

2.10 Experimental condition 25

3 Data Analysis **28**

3.1 Particle identification 28

3.2 Track reconstruction 29

3.3 Scattering angle calibration 30

3.3.1 Obtaining the information of sieve-slit images 30

3.3.2 Study of the suitable function to reconstruct scattering angle 31

3.3.3 Correction of beam position in the vertical direction 35

3.3.4 Adequacy of the reconstructing function 36

3.4 Calibration of the GR ion-optics and kinematical effect 36

3.5 Background subtraction 37

3.5.1 Focusing in the vertical direction 41

3.5.2 Background subtraction 43

3.6 Energy calibration 45

3.7 Elastic scattering 45

3.7.1 Beam polarization 45

3.7.2 Differential cross section and analyzing power 46

4 Results **48**

4.1 Reduction of cross section 48

4.1.1 Excitation energy spectra 48

4.1.2 Peak fitting 49

4.1.3 Differential cross section 49

4.2 Optical potential 52

4.2.1 Beam polarization 52

4.2.2 Calibration of target thickness 53

4.2.3 Optical potential 53

5 Extraction of B(σ) strength **55**

5.1 Shell model calculation 55

5.2 DWBA calculation 56

5.3 J^π and isospin assignments . . . 56
5.3.1 1^+, T = 0 (isoscalar) states . . . 57
5.3.2 1^+, T=1 (isovector) states . . . 58
5.3.3 0^+ states . . . 58
5.3.4 Contaminations from other isotopes . . . 62
5.4 Unit cross section for B(σ) . . . 62
5.4.1 Formula of unit cross section . . . 62
5.4.2 Kinematical factor $F(q, \omega)$ . . . 62
5.4.3 Obtained unit cross section for B(σ) . . . 63
5.5 Conversion to B(σ) strength . . . 66
5.5.1 Extrapolation to $\theta_{cm} = 0^\circ$ . . . 66
5.5.2 Extrapolation to energy transfer $\omega = 0$ MeV . . . 66
5.5.3 Obtained B(σ) strength . . . 66

6 Discussion **68**
6.1 Strength fragmentation . . . 68
6.2 Total sum of the strengths . . . 70

7 Conclusion **72**

A Unit cross section check of ^{12}C **74**
A.1 Deduction of experimental value . . . 74
A.2 Consistency check of the unit cross section . . . 77

Chapter 1

Introduction

Spin-isospin excitations in nuclei have been the subject of theoretical as well as experimental work for the study of nuclear structures over the past decades. Experimentally, hadronic reactions in the intermediated energy region of 100−500 MeV/u have played an important role. In the present study, we focus our attention on the magnetic dipole ($M1$) excitation (ΔL = 0, ΔS = 1) which includes both isoscalar (ΔT = 0) and isovector (ΔT = 1) transition.

1.1 Quenching problem

1.1.1 GT quenching problem

The quenching problem of Gammow-Teller (GT) strengths with respect to " Ikeda sum rule" [1] has been discussed for a long time as an opened question. The problem is that a sum of observed strengths in GT transition does not exhaust the sum rule value which is deduced from the permutation relationship of the isospin raising and lowering operators. This is a model-independent value. Here the sum rule for the GT strength S_{GT} is given by the following equation

$$S_{GT} = S_{\beta-} - S_{\beta+} = 3(N - Z), \tag{1.1}$$

where $S_{\beta-}$ and $S_{\beta+}$ are total GT^- and GT^+ strengths, respectively and N and Z are neutron and proton numbers, respectively [1]. The quenching factors which were defined as the ratio of an experimentally observed value to the sum rule value were 50−60% for various nuclei [2]. Two physical mechanisms were proposed in order to understand the

quenching of the GT strength. One was Δ-hole admixture into the one-particle-one-hole ($1p1h$) GT state [3]. The other was the configuration mixing with the $2p2h$ configurations or the many-particle-many-hole ones [4]. Recent sophisticated studies in both (p,n) and (n,p) reactions have revealed that a significant amount of the missing GT strength is located in the continuum region up to $E_x = 50$ MeV, which exhausts about 90% of the GT sum rule [5, 6]. These results indicate that the quenching problem of the GT strengths is mainly due to the mixing of the $2p2h$ or the many-particle-many-hole configurations.

1.1.2 $M1$ quenching problem

The $M1$ transition (ΔL = 0, ΔS = 1, ΔT = 0 or 1) is similar to the GT one (ΔL = 0, ΔS = 1, ΔT = 1) because they are mediated mainly by the common operator $\vec{\sigma}\vec{\tau}$. Based on being mediated by the same operator, the quenching problem can be studied also in the $M1$ strength.

Anantaraman *et al.* [7] studied the $M1$ quenching in ^{28}Si(p,p') reactions at $E_p = 201$ MeV at Orsay. They measured angular distributions of cross sections at $\theta_{lab} = 3{-}12^\circ$. The theoretical curve was multiplied by normalizing factor to be fit the measured cross sections. The average values of the normalizing factors were taken as quenching factor. They were 0.24 (0.33) for isoscalar (isovector) excitations.

Five years later, Crawley *et al.* [8] of the same group with Anantaraman *et al.* performed systematic studies of (p,p') measurements at the same facility using various *sd*-shell nuclei. They also measured angular distribution at $\theta_{lab} = 3{-}12^\circ$. The measured cross sections were extrapolated to at small momentum transfer ($\theta = 0^\circ$) by applying the theoretical angular distribution. They calculated the ratio of the theoretical B(σ) value to the theoretical cross section at 0°. The average value of this ratio was applied to the experimental cross sections in order to deduce the B(σ) value. They compared the observed total strength with the predicted one because it was more reliable than to try to make comparisons state by state. Their results are shown in Fig. 1.1. The quenching factors for ^{28}Si were 0.50 ± 0.10 (0.79 ± 0.10) for isoscalar (isovector) excitations. They concluded that almost no quenching was observed.

In Crawley's spectra, however, a large amount of background lay in. It brought fairly

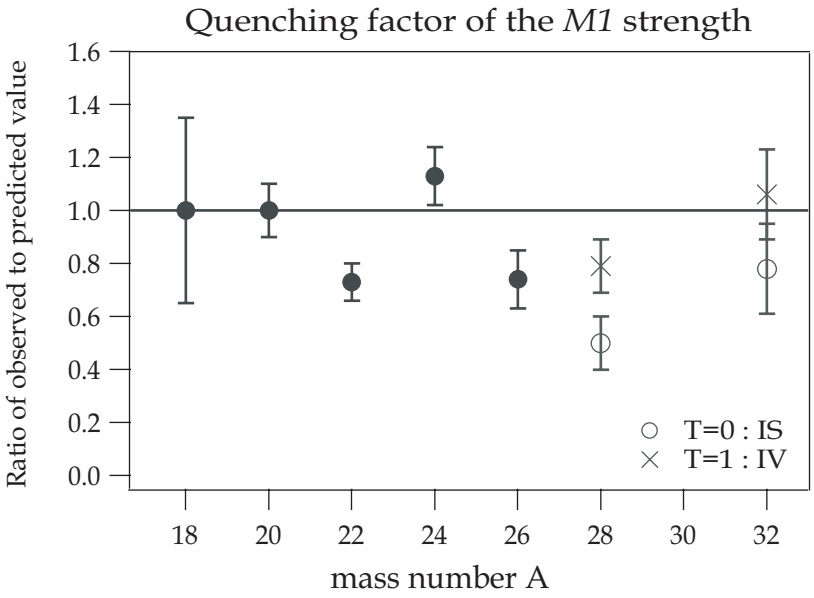

Figure 1.1: $M1$ quenching factors taken from Ref. [8] and references therein. The quenching factors of total strength of the isoscalar and the isovector excitations are drawn as filled circles. The results for the nuclei of A = 28, 32 which are ^{28}Si and ^{32}S, respectively, are separately drawn as the isoscalar strength quenching (ΔT = 0) and the isovector one (ΔT = 1). Almost no quenching is observed even though the factors are fluctuating from unity.

uncertainty to extract the cross sections. For some states, the theory failed to reproduce the slope making it difficult to extrapolate the measured angular distribution to 0°. Additionally, uncertainties as large as 20% resulted from converting the cross sections to B(σ). These ambiguities should be reduced for a reliable discussion on the $M1$ quenching problem.

1.2 Isoscalar and isovector transition of $M1$

In the $M1$ excitation, there are two types of transitions : isoscalar (ΔT = 0) and isovector (ΔT = 1) ones. This is one of interesting points in the $M1$ excitation. Although the Δ-hole admixture is proposed as one of the GT quenching mechanisms, it cannot occur in an isoscalar excitation. It is understood that the $\Delta(1232)$ has an isospin quantum number of 3/2 and couples to $3/2 \oplus 1/2 = 1$ or 2 with respect to the isospin, which never results in $T = 0$. The behaviors of the two proposed mechanisms in the $M1$ excitation are summarized in Table 1.1. According to this table, the isovector strength quenches more

Table 1.1: The behaviors of the two proposed quenching mechanisms in $M1$ excitations. Although the $2p$-$2h$ configurations or the np-nh ones occurs in both isoscalar and isovector transitions, the Δ-hole admixture never occurs in an isoscalar transition owing to the isospin quantum number of 3/2 the $\Delta(1232)$ particle.

	isoscalar (ΔT = 0)	isovector (ΔT = 1)
Δ-hole	impossible	possible
$2p$-$2h$	possible	possible

than the isoscalar one. As shown in Fig. 1.1, however, Crawley found a tendency that $T = 0$ states are more quenched than $T = 1$ states, which indicated the opposite trend to the anticipation. Failing for some states to be assigned the correct J^π and the isospin might cause the unexpected tendency. It was due to relatively poor energy resolution.

1.3 Essential points for obtaining conclusive results

At 0°, ΔL = 0 excitations are enhanced the most. For a reliable conversion, the (p, p') cross section at small momentum transfer ($\theta_{c.m.} \approx 0°$) is to be converted to B(σ). Crawley *et al.* took the energy spectra at a laboratory angle of 3° because measuring inelastic scattering events at 0° was difficult. A huge background comes mainly from multiple scattering of the primary beam at the target.

In order to deduce accurate B(σ), the (p, p') experiment at the very zero-degrees is essential. In addition to a reliable extrapolation of the cross section to 0°, a good energy resolution to separate peaks and a reasonable background subtraction are also essential for conclusive results about the $M1$ quenching.

1.4 Purpose of this work

The purpose of this work is to obtain a precise B(σ) strength and to study a strength fragmentation for both isoscalar and isovector excitation in ^{28}Si using a (p, p') reaction. The measurement at 0° with high resolution is essential. For this purpose, we have performed the experiment at the RCNP WS course [9]. This facility has achieved (p, p') measurements at 0° with reasonable background subtraction [10, 11, 12] and high resolution study of (^{3}He,t) reactions has been intensively performed [13, 14]. Since, however, (p, p') mea-

surements at 0° with high resolution is performed for the first time, establishment of the new tool is also the purpose of this work.

In Chap. 2, the experimental setup and conditions are described. The procedure of the data analysis to reconstruct energy spectra is explained in Chap. 3. The experimental results are presented in Chap. 4. Chapter 5 is devoted to a description for selecting $M1$ excitations and for obtaining $\mathrm{B}(\sigma)$ strengths. In Chap. 6, the total sum and the fragmentation of the strength are compared with theoretical ones and discussions on them are given. Finally, the conclusions are given in Chap. 7.

Chapter 2

Experimental Methods

The experiment was carried out at the Research Center for Nuclear Physics (RCNP) , Osaka University using 295 MeV unpolarized/polarized proton beams. An overview of the RCNP facility is illustrated in Fig. 2.1. Protons accelerated by the coupled cyclotrons were transported to the high resolution beam line, WS course [9]. For a high energy resolution, *dispersion matching technique* [15] was applied to the WS course. Protons scattered by a target placed in the scattering chamber were analyzed by two spectrometers; one was *Grand Raiden* (GR) [16] which was used as the main spectrometer in the present experiment and the other was *Large Acceptance Spectrometer* (LAS) [17]. Three kinds of measurements were done for the present experiment. Beam polarization mode and spectrometers which were used for each measurement are followings :

- Forward angle scattering measurements (main experiment) : unpol, GR, LAS
- Sieve slit measurements : unpol, GR, LAS
- Elastic scattering measurements : pol, GR

Detailed conditions of each measurement are summarized in Sec. 2.10.

The beam time was divided into two parts; the first experiment was carried out in October 2004 and the second one was in July 2005.

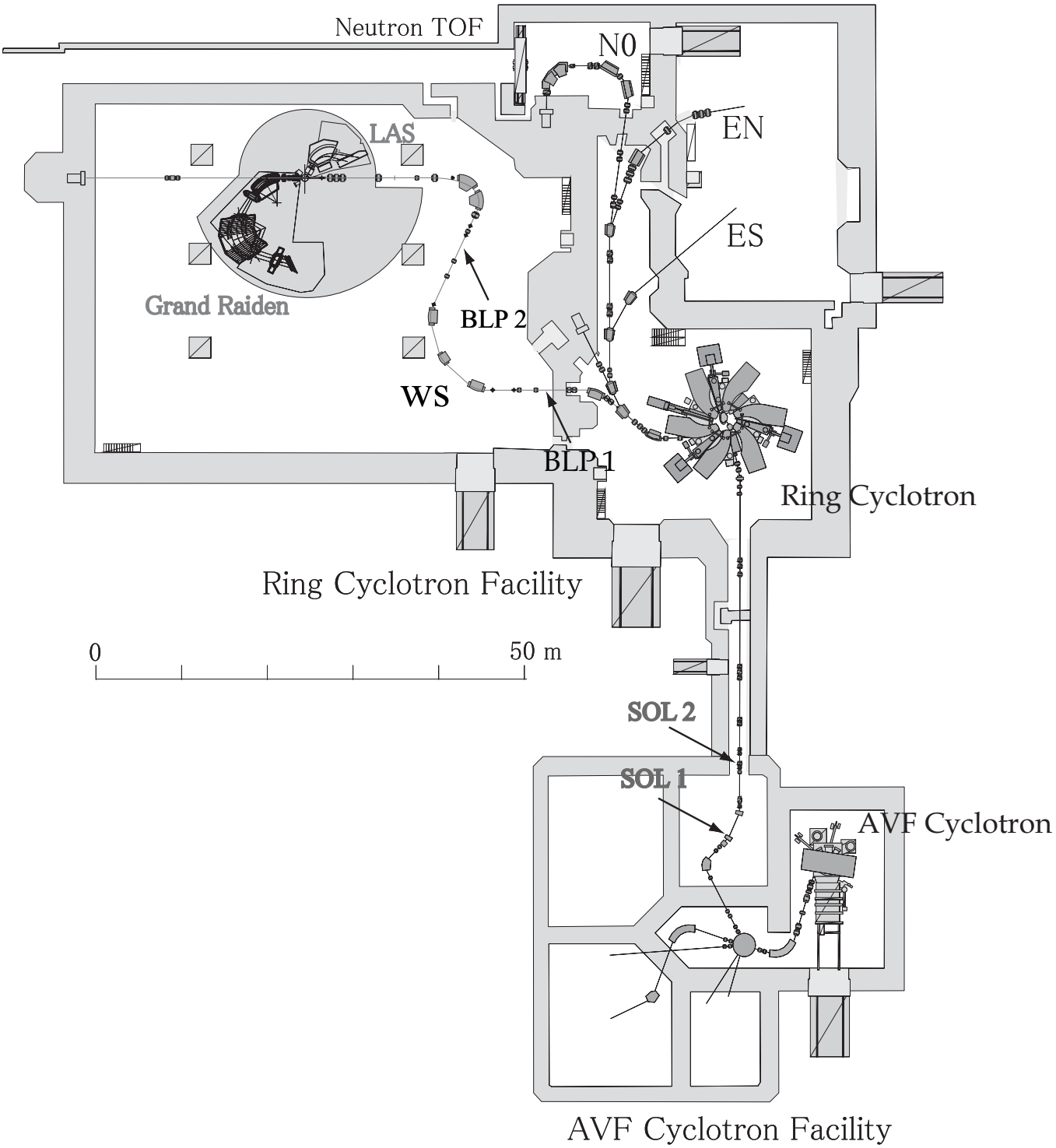

Figure 2.1: A schematic view of Research Center for Nuclear Physics (RCNP)

2.1 Ion source

2.1.1 Unpolarized ion source

An ECR (Electron Cyclotron Resonance) ion source made of permanent magnets, named NEOMAFIOS [18], was operated at 10 GHz for providing unpolarized proton beams. Ions were vertically injected into the AVF (Azimuthally Varying Field) cyclotron through the axial injection line. Typical beam intensity was 3-4 nA on target for the 0° measurement and 6-10 nA for forward and finite angles measurements.

2.1.2 Polarized ion source

A polarized proton beam was provided by the High Intensity Polarized Ion Source (HIPIS) [19]. The HIPIS is a polarized ion source of atomic beam type. The polarized proton beam extracted from the HIPIS was bent from the horizontal direction to the vertical direction by an electrostatic deflector and a dipole magnet, and was injected to the AVF cyclotron with the polarization axis in the vertical direction. In order to cancel out geometrical asymmetries in the experimental apparatus, the nuclear polarization state was toggled between the normal and reverse states in every second. The HIPIS was used only for elastic scattering measurements in order to measure analyzing power for optical potential. Typical beam intensity was 5-10 nA on target in the present experiment.

2.2 Beam Line Polarimeter (BLP)

The polarization of the proton beam was measured by a set of beam line polarimeters (BLPs). Setup of the BLP is illustrated in Fig. 2.6. A polyethylene sheet with a thickness of 19.4 mg/cm^2 was used as the analyzer target. The proton scattered elastically or quasi-elastically from analyzer target and recoiled one were detected in coincidence by plastic scintillation counters. Two pairs of the plastic scintillation detectors (R-R' and L-L' in Fig. 2.6) were placed in the horizontal plane to measure right/left scattering asymmetry.

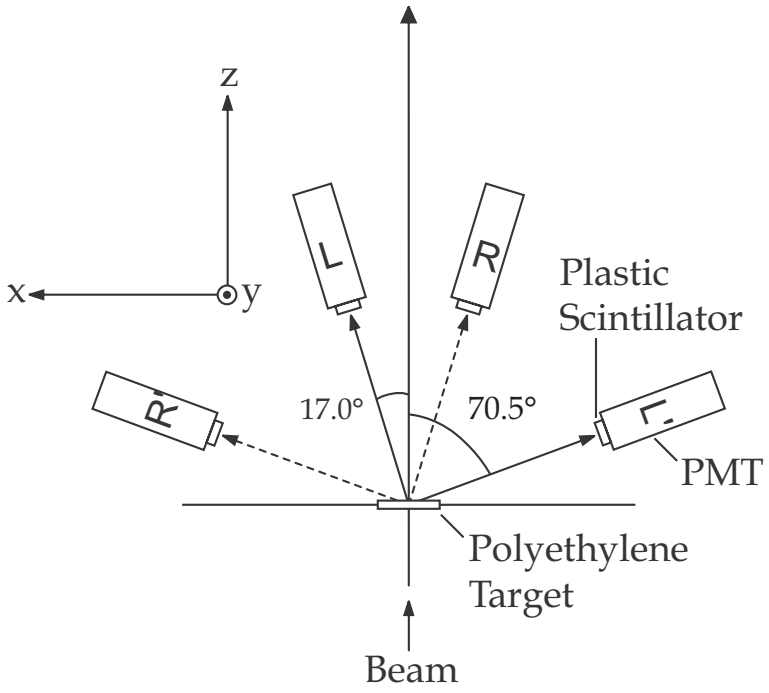

Figure 2.2: Setup of the plastic scintillation counters for the BLP in the horizontal plane.

2.3 Target

Two ^{28}Si targets were prepared. The natural abundance of ^{28}Si was 92.2 %. One was a thin foil with a thickness of 2.22(2) mg/cm^2, and the other was a wafer with a thickness of 58.5 mg/cm^2. Thinner one was used for high resolution measurements and its thickness was calibrated by using the wafer because of its homogeneity. The detail of the calibration procedure will be described in Sec. 4.2.2. The wafer target was used in the elastic scattering measurement at finite angles with an expectation of higher statistics because the cross section fell down with increasing the scattering angles.

2.4 Magnetic spectrometers

A setup of 0° measurement is shown in Fig.2.3 as an example of a schematic view of the two-arm spectrometer system at RCNP.

2.4.1 Grand Raiden (GR)

The spectrometer *Grand Raiden* (GR) [16] was designed for high resolution measurements. The GR has a QSQDMDD configurations : three dipole (D1, D2 and DSR) mag-

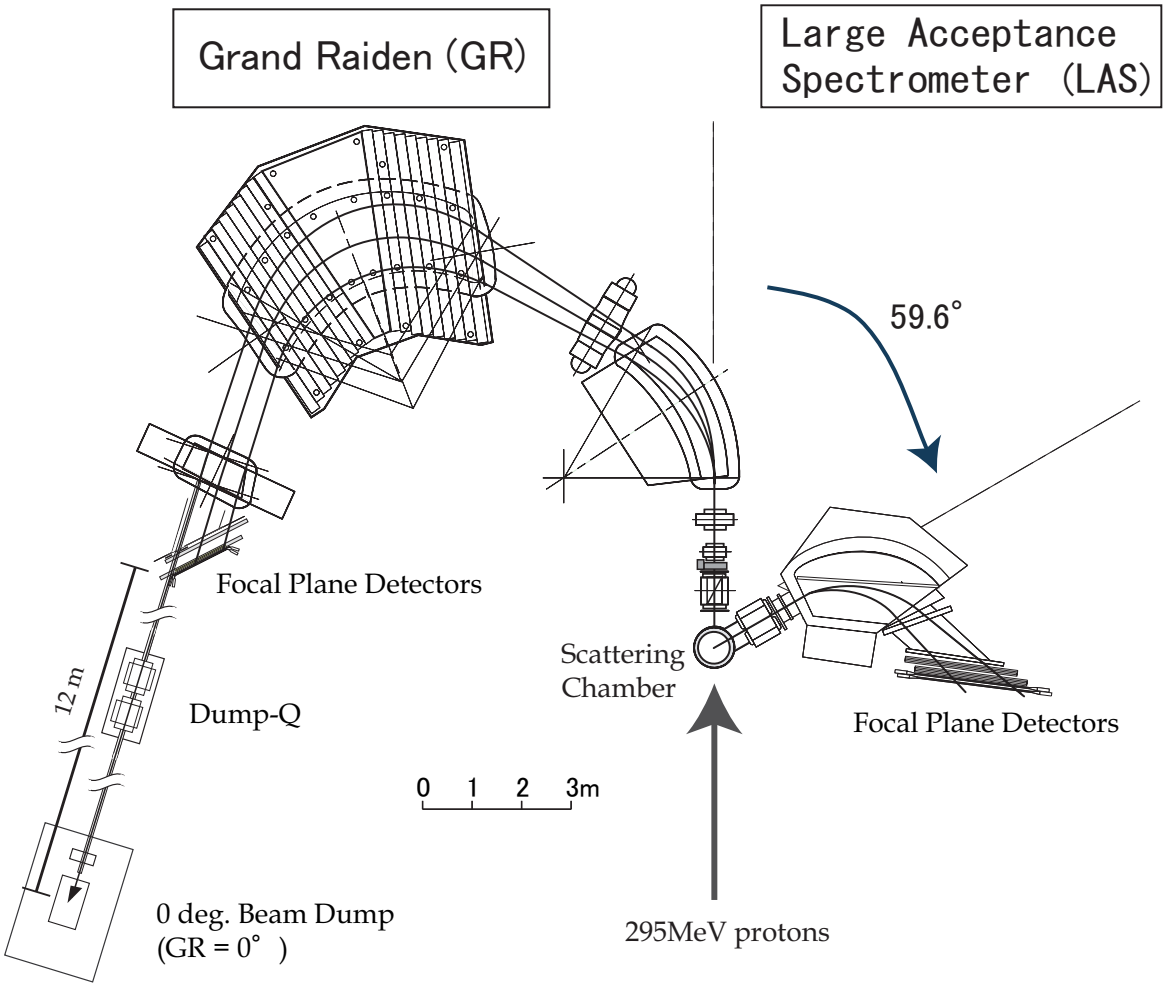

Figure 2.3: Schematic view of the two-arm spectrometer in the setup of 0° measurement.

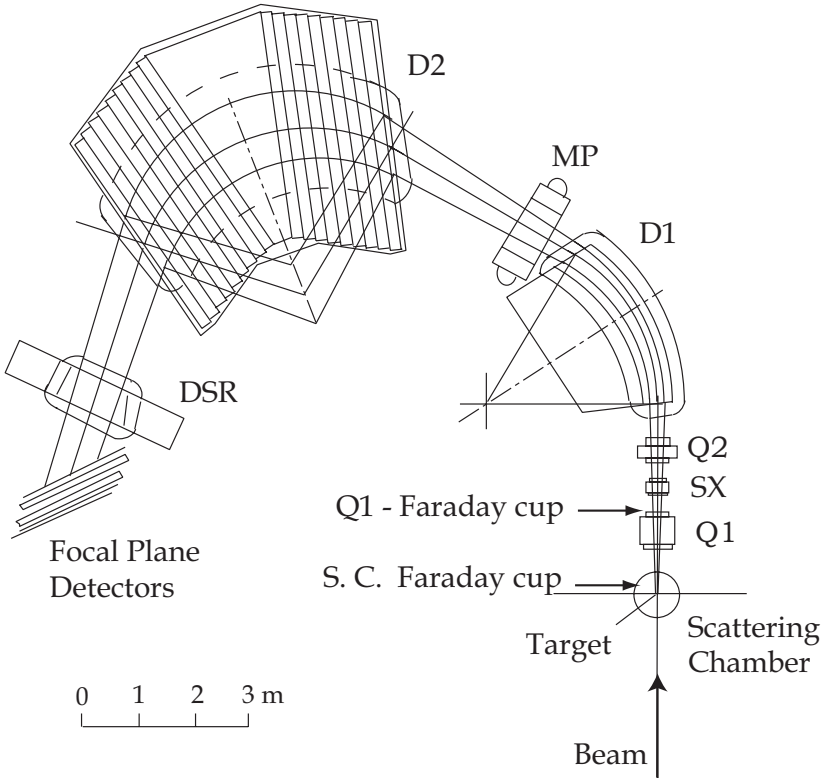

Figure 2.4: Over view of high resolution spectrometer Grand Raiden (GR). There are S. C. Faraday cup in the scattering chamber and Q1 Faraday cup in the Q1 magnet.

nets, two quadrupole (Q1 and Q2) magnets, a sextupole (SX) magnet and a multipole (MP) magnet (Fig.2.4). The designed specifications of the GR are summarized in Table 2.1. One of the remarkable characters is its high momentum resolution of $p/\Delta p = 37076$.

2.4.2 Large Acceptance Spectrometer (LAS)

Large Acceptance Spectrometer (LAS) [17] is a QD type spectrometer with large angular and momentum acceptances (Fig.2.5). The design specifications are summarized in Table 2.1. The LAS was fixed at $\theta_{lab} = 59.6^\circ$ during the present experiment and was used as a beam spot monitor in the vertical direction. For the LAS, this was the most forward angle when the GR was placed at zero degrees (Fig. 2.3). The LAS detected quasi-free scattered protons mainly and these data were useful for calibrating the vertical scattering angle of protons measured by the GR which sensitively depended on the beam position in the vertical direction. A tapered collimator made by Sagara group[1] was set at 580 mm

[1]Kyusyu University, Japan

Table 2.1: Specification of two spectrometers.

	Grand Raiden (GR)	Large Acceptance Spectrometer (LAS)
Configuration	QSQDMDD	QD
Mean orbit radius	3m	1.75m
Total deflection angle	162°	70°
Tilting angle of focal line	45°	57°
Maximum magnetic rigidity	5.4 T·m	3.2 T·m
Veritical magnification	5.98	-7.3
Horizontal magnification	-0.417	-0.4
Momentum range	5 %	30 %
Momentum resolution	37076	4980
Acceptance of horizontal angle	±20 mr	±60 mr
Acceptance of vertical angle	±70 mr	±100 mr

downstream of the target, and it limited scattered protons in opening angles of ±69 mrad (horizontal) and ±6.9 mrad (vertical).

For the measurement of elastic scatterings using a polarized beam, the LAS was not used because data collimated by a slit in one-shot of the GR were not divided. The vertical scattering angle information was not necessary for the elastic scatterings analysis.

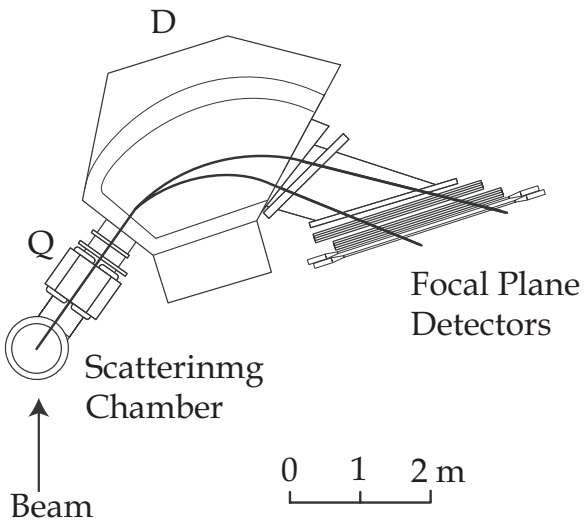

Figure 2.5: Over view of Large Acceptance Spectrometer (LAS)

2.5 Focal plane detector system of GR

The focal plane detector system of the GR consisted of two multi-wire drift chambers (MWDC) of vertical drift type (VDCs) [20] and a couple of plastic scintillation counters (PS1 and PS2). A schematic view of the detector system is shown in Fig. 2.6.

The VDCs were used to determine trajectory of protons at the focal plane. The structure of one wire plane of a VDC is shown in Fig. 2.7 and the specifications are summarized in Table 2.2. Each VDC consisted of two anode wire planes (X and U). The configuration and the structure of each wire plane are illustrated in Fig. 2.7 and 2.8. High voltage of -5.6 kV was applied to the cathode planes of the VDCs. Voltages of -0.35 kV were applied to the potential wires in the X and U planes for better efficiencies of a VDC. A gas mixture of Argon (70%), Iso-butane (30%), and Iso-propyl-alcohol (vapor pressure at 2 ℃) was used. Signals from the anode wires were pre-amplified and discriminated by LeCroy 2735DC cards. Timing information was digitized by using LeCroy 3377 drift chamber TDCs.

Two plastic scintillators with a thickness of 10 mm placed at downstream of the VDCs were used as the GR trigger scintillators (PS1 and PS2). An aluminium plate of 10 mm thickness was set between PS1 and PS2 in order to absorb electrons knocked out by Compton scattering. The scintillation light was detected by the PMTs on both sides of each PS. Signals from the Photomultiplier's tubes (PMT's) were digitized by the LeCroy FERA and FERET systems and were recorded by the data acquisition system [21].

2.6 Focal plane detector system of LAS

The focal plane detector system of the LAS consisted of two VDCs [22] and two planes of plastic trigger scintillators (PS1 and PS2). The detector layout is shown in Fig. 2.9.

The VDCs for the LAS were similar to those of the GR. The different point was that each VDC consisted of three anode wire planes (Fig. 2.10). The X-U planes were used in the experiment performed at October 2004 and the U-V planes were at July 2005. The configuration of U-V planes was expected to provide a better resolution of particle trajectories. A high voltage of -5.5 kV was applied to the cathode planes, and -0.5 kV

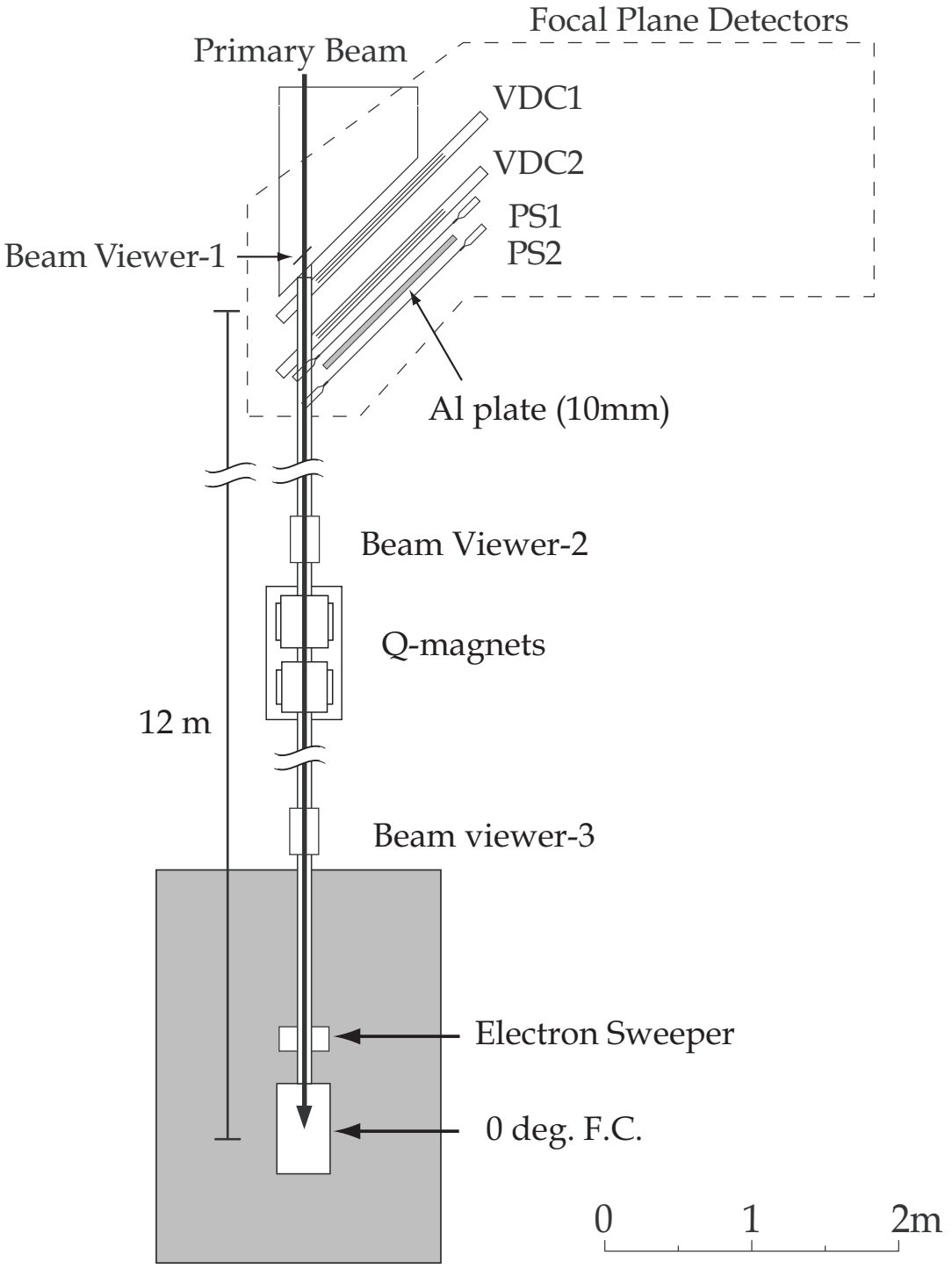

Figure 2.6: The focal plane detector system of the GR and the beam line to the Faraday cup for the 0° measurement.

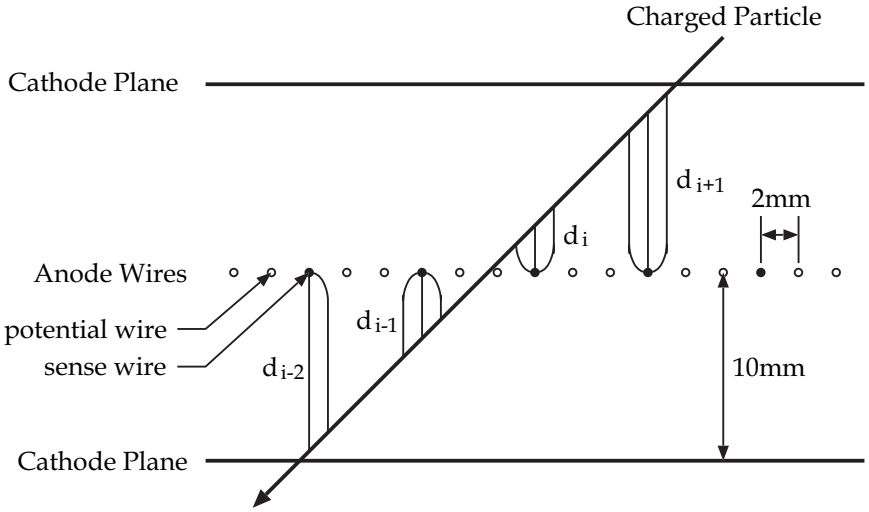

Figure 2.7: Schematic figure of a plane of VDCs. Cathode planes and anode wires are illustrated together with a typical charged particle track.

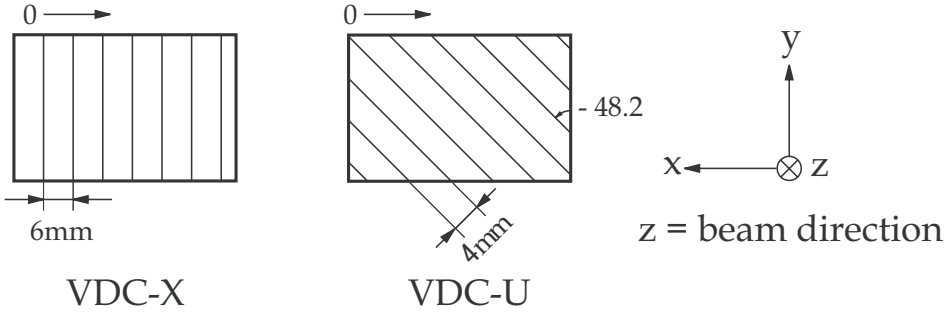

Figure 2.8: Wire configuration of the GR VDCs.

Table 2.2: Specifications for the GR VDCs.

Wire configuration	X(0°=vertical), U(48.2°)
Active area	$1150^{w} \times 120^{H}$ mm
Number of sense wires	192 (X), 208 (U)
Cathode-anode gap	10 mm
Anode wire spacing	2 mm
Sense wire spacing	6 mm (X),4 mm (U)
Sense wires	20μmϕ gold-plated tungsten wire
Potential wires	50μmϕ beryllium-copper wire
Cathode	10μm carbon-aramid film
Cathode voltage	-5.6 kV
Potential-wire voltage	-0.35 kV
Gas mixture	Argon(70%) + Iso-butane(30%)
	+ Iso-propyl-alcohol(vapor pressure at 2 ℃)
Gas seal	12.5 μm aramid film
Pre-amplifier	LeCroy 2735DC
TDC	LeCroy 3377

to the potential wires. The specifications of the VDCs are summarized in Table 2.3.

The trigger scintillator system consisted of two planes of plastic scintillators (PS1 and PS2). Each of PS1 and PS2 consisted of three scintillation counters of 196 × 15 × 0.6 cm^3 to cover the whole area of the focal plane. Note that only the middle counters of PS1 and PS2 were used for the present experiment because scattered protons to be measured were collimated in a small solid angle by the slit. The layout is shown in Fig. 2.9.

2.7 Faraday cup and beam line for the 0° measurement

The schematic view of the setup for 0° measurements is shown in Fig. 2.6. This setup was used only for the 0° measurement. The vacuum ducts to the 0° dump were removed and the GR was rotated for finite angles measurement at 2.5°, 4.5°, etc.

Three beam monitors were used for a detailed beam tuning which will be explained in Sec. 2.8. Before being transported to a 0° Faraday cup, the beam was focused by a couple quadrupole magnet after passing through the GR and VDCs. The upstream magnet focused the beam in horizontal direction because a beam spot of the dispersive mode was broad in the dispersive direction.

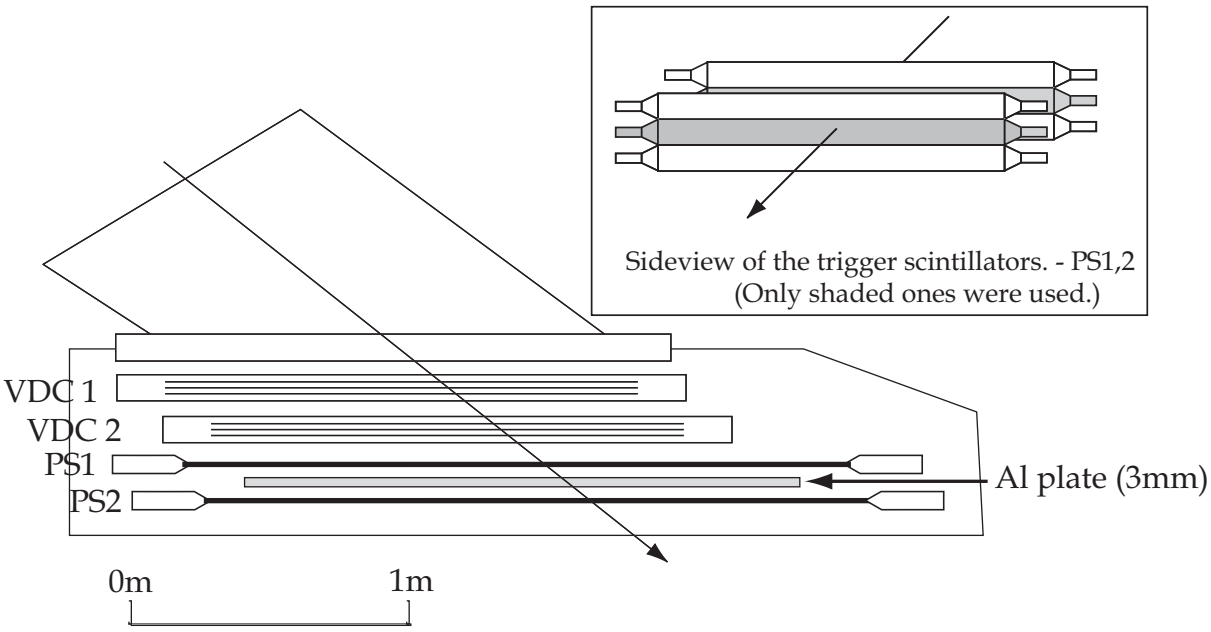

Figure 2.9: The focal plane detectors of the LAS.

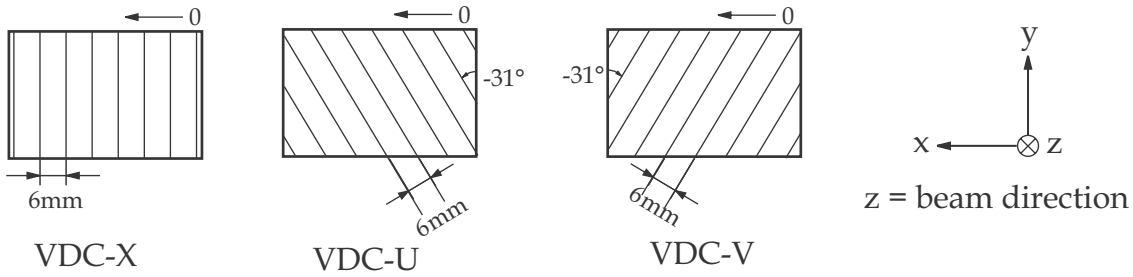

Figure 2.10: Wire configuration of the LAS VDCs.

Table 2.3: Specifications for the LAS VDCs.

Wire configuration	X(0°=vertical), U(-31°) , V(+31°)
Active area	$1700^{w} \times 350^{H}$ mm
Number of sense wires	272 (X), 256 (U, V)
Cathode-anode gap	10 mm
Anode wire spacing	2 mm (X), 2.33 mm (U,V)
Sense wire spacing	6 mm (X), 7 mm (U,V)
Sense wires	20μmϕ gold-plated tungsten wire
Potential wires	50μmϕ beryllium-copper wire
Cathode	10μm carbon-aramid film
Cathode voltage	-5.5 kV
Potential-wire voltage	-0.5 kV
Gas mixture	Argon(70%) + Iso-butane(30%)
	+ Iso-propyl-alcohol(vapor pressure at 2 ℃)
Gas seal	25 μm aramid film
Pre-amplifier	LeCroy 2735DC
TDC	LeCroy 3377

The primary beam was stopped in the 0° Faraday cup which was placed at 12 m downstream of the focal plane. The Faraday cup was shielded by lead blocks and was surrounded by concrete blocks of which size was 2×3 m^2 in total as a beam dump. The distance of 12 m from the Faraday cup to the focal plane detectors and shielding by lead and concrete blocks were effective for reducing background events. At the entrance of the beam dump, an electron sweeper to bend out electrons by magnetic fields was placed for measuring the beam current correctly.

2.8 Beam tuning

For the measurement of inelastically scatterings at forward angles including zero-degrees, a halo-free beam is essential since huge background events come to the detector system from the beam halo. Here, halo-free beam means a narrow width of energy spreading of itself. In this section, the procedure of beam tuning required for high resolution measurements at 0° is described.

One of the key points for high quality beam was a stable condition of single turn extraction from the injector AVF cyclotron, while those of the RING cyclotron was at a level of satisfaction [23]. By accelerator group's efforts, turn patterns in the AVF cyclotron

which were observed by a beam probe showed good separation and it was not hard to perform single turn extraction (Fig. 2.11). After single turn extraction from both the AVF and RING cyclotrons, the beam was transported to the WS course with achromatic transport mode. The beam was tuned to achieve an energy resolution of 37 keV in FWHM for elastic scatterings at 8° on ^{197}Au target with a thickness of 1.68 mg/cm^2. Then, the GR was rotated to 0° and the beam was guided to the 0° Faraday cup with referring three beam viewers and adjusting magnetic fields of the D1, D2 and DSR holding the ratio of the D1 and D2. By halo-free tuning, the trigger rate of the GR was reduced from more than 1000 cps to 50 cps with an empty target frame at 1 nA beam current. The slits and Q-magnets at the injection line from the AVF cyclotron to the RING were adjusted mainly for halo-free beam tuning. The transport mode was changed to dispersive mode and a matching condition was searched by detecting a faint beam itself [15]. In the best matching condition, a faint beam energy resolution of 12 keV in FWHM was finally achieved. This energy width of the faint beam corresponded to a spot size of 3 mm on the target in the dispersive direction (Fig. 2.12). It took about 2 days totally for the tuning.

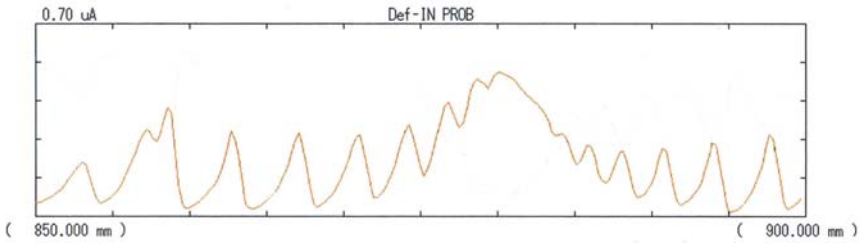

Figure 2.11: Turn patterns in the AVF cyclotron measured by a beam profiling probe. The turn extraction radius is located around the right edge of the histogram.

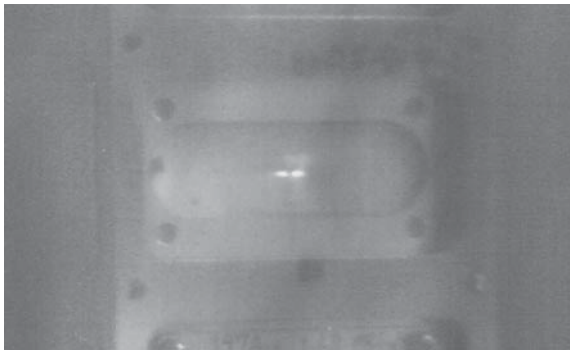

Figure 2.12: Beam spot on the target in the dispersive transport mode.

2.9 Under-focus mode

2.9.1 Purpose and principle

Under-focus mode was applied for a good scattering angular resolution, while *dispersion matching technique* [15] was performed for a better energy resolution. For the precise determination of a scattering angle around zero-degrees, both horizontal and vertical components were equally important because their relationship was expressed as $\Theta_{total} = \sqrt{{\theta_{tgt}}^2 + {\phi_{tgt}}^2}$, where Θ_{total} was total scattering angle and θ_{tgt} (ϕ_{tgt}) was scattering angle in the horizontal (vertical) direction. However the GR didn't have a good vertical angle resolution although they both had to be measured in a good accuracy. In order to improve a scattering angle resolution without losing the large acceptance in vertical direction, the magnetic fields of the GR were set at off-focus mode by modifying the strength of the quadrupole magnet Q1 of the GR. This defocusing means that the focal plane in the vertical direction is shifted from the detector position to upstream or downstream, which is called over-focus mode or under-focus mode, respectively (Fig. 2.13) [24] . In the present experiment, we chose mildly under-focus mode because over-focus mode appeared to have larger correlation between the vertical and horizontal scattering angles at the detector plane.

Under the measurement of under-focus mode, the vertical scattering angle at the target (ϕ_{tgt}) was measured as the vertical position at the detector plane (y_{fp}) instead of measuring ϕ_{tgt} itself because of the small angle magnification of ϕ_{tgt}, 0.17. This small magnification results in bad resolution. A ray-trace from a hole of the sieve-slit to an observed image of the θ_{fp}-y_{fp} plane (horizontal scattering angle versus vertical position at detector position) was performed in order to know the function to connect the relationship between θ_{fp}-y_{fp} plane and θ_{tgt}-ϕ_{tgt} one. Since we knew distances of between holes of the sieve-slit and the target placed in the scattering chamber, values of the scattering angle at the target in both components, θ_{tgt} and ϕ_{tgt}, were deduced by using the relationship. Once the function was deduced, we could reconstruct θ_{tgt} and ϕ_{tgt} without measuring ϕ_{tgt} itself.

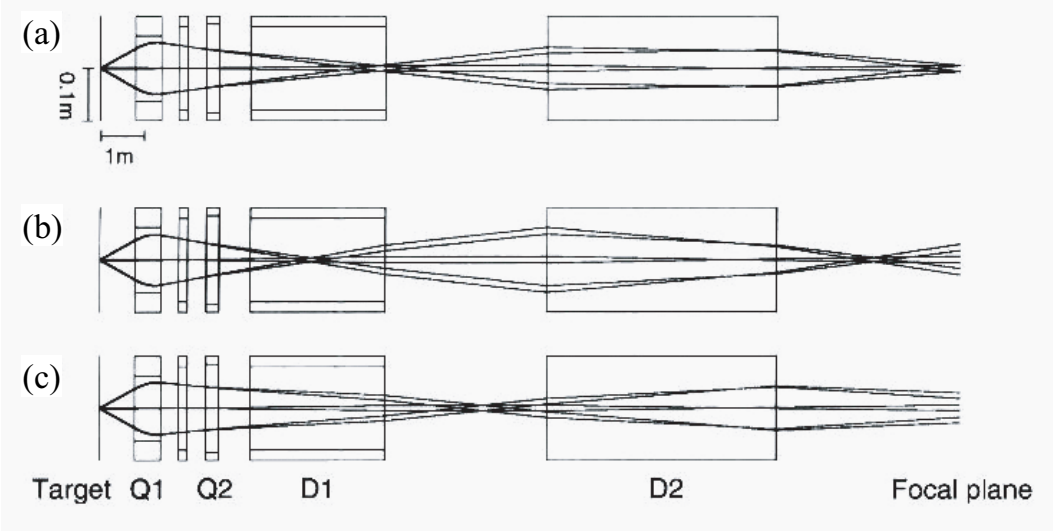

Figure 2.13: Vertical component of the beam envelope of analyzed particles in the GR [24]. (a)Normal-focus mode. (b)Over-focus mode. (c)Under-focus mode.

2.9.2 Sieve-slit Measurement

In order to know the function to reconstruct θ_{tgt} and ϕ_{tgt}, sieve-slit measurement was employed as described in the following.

A brass plate of 5 mm thickness was used as the sieve-slit, which had 25 holes in total, vertically and horizontally 5 × 5 holes (Fig. 2.14). The sieve-slit was positioned 638 mm downstream of the target, where is an entrance of the GR. The separation of holes between each corresponded to 4.5 (12) mrad of the scattering angle of the horizontal (vertical) component. Diameters of each hole were 3.1 mrad (2 mmϕ) except that of the center hole was 4.7 mrad (3 mmϕ) for recognizing the position. A ^{58}Ni target of 100.1 mg/cm^2 thickness was used. The GR was placed at $\theta_{lab} = 14^\circ$ with an expectation of less ambiguity of the scattering angle, where the differential cross section of ^{58}Ni(p, p_0) reaction had more or less flat angular distribution. Measurements around the minimum or maximum point of an angular distribution had an expectation of less ambiguity in the scattering angle. The beam was transported in the achromatic mode. Since this angle calibration is very sensitive to the beam position, several data of different beam positions were taken, which were 15 runs in total. A beam spot was swung to 0 and ±1 mm in vertical direction and 0, ±4 and ±8 mm in horizontal direction on the target. The LAS was also used as a beam spot monitor in the vertical direction. Protons which

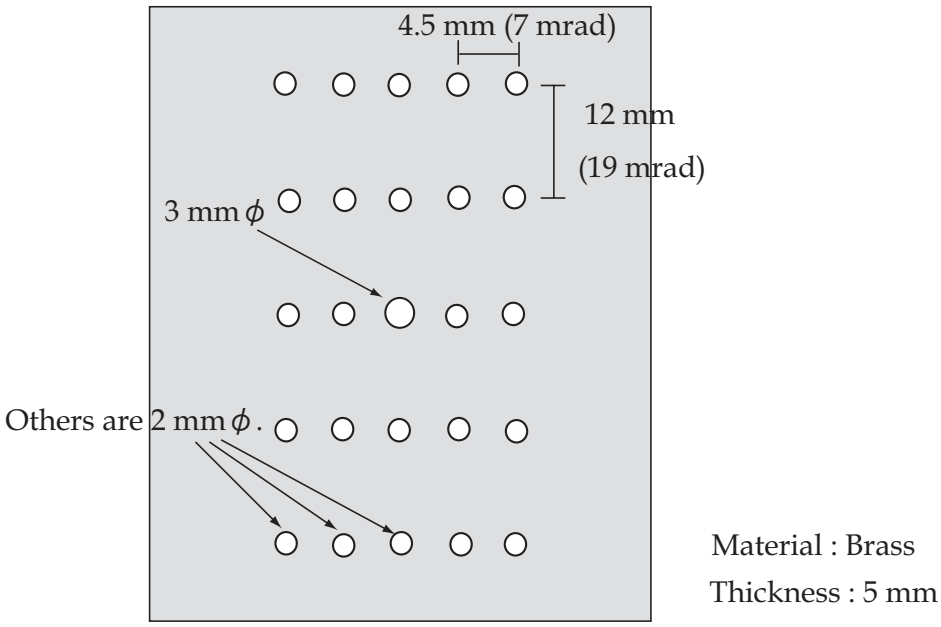

Figure 2.14: Schematic view of the sieve-slit. Diameters of each hole are 3.1 mrad (2 mmϕ) except that of the center hole is 4.7 mrad (3 mmϕ) for recognizing the position.

passed one of the holes of the slit after being elastically scattered at the target were selected by software. Three runs with different magnetic field settings were performed, which were set at +1.0%, +2.5% and +4.0% relative to the values of a normal zero-degree measurement. These magnetic fields guided elastic scattering events to x_{fp} positions which corresponded to the 6, 13 and 20 MeV of the excitation energy in the magnetic fields of the 0° measurement, respectively. From these three data, ion optical parameters of the GR was calibrated as the function depending on the horizontal position (x_{fp}).

2.10 Experimental condition

The experimental conditions are summarized in Table 2.4 and Table 2.5. The beam was transported in the dispersive mode except for the elastic scattering measurement. No slit was used for 0°, 2.5° and 4.5° measurements in order not to arise background events due to scattering at the slit. The slit of ±20 mr × ±30 mr was used for finite angles measurements and elastic scattering measurements for determining the acceptance precisely. Typical time of measurements for each angle were 12 hours at 0°, 3 hours at 2.5°, 90 min. at 4.5 °, 60 min. for finite angles measurements and 3−20 min. for elastic measurements. In the forward angle measurements except 0°, the beam was stopped by the Faraday cup

in the Q1 magnet of the GR. In other finite angle measurements and elastic scattering measurements, the Faraday cup in the scattering chamber was used, which was called S.C. Faraday cup. The location of these Faraday cups was shown in Fig. 2.4. The consistency among 0°, Q1 and S.C. Faraday cups, was checked by normalizing the beam current yields by BLPs counts without chance events. Their results were summarized in Table. 2.6. The differences among them were less than a few percentage.

Table 2.4: Summary of the common experimental conditions.

beam	proton	
beam energy	295	MeV
target	^{28}Si	
target thickness (thin)	2.22	mg/cm^2
target thickness (wafer)	58.5	mg/cm^2
abundance of ^{28}Si	92.2	%
energy resolution (achromatic)	37	keV
energy resolution (disp. with faint beam)	12	keV
LAS angle (lab.)	59.6	deg
LAS horizontal acceptance (lab.)	69	mrad
LAS vertical acceptance (lab.)	6.9	mrad

Table 2.5: Summary of the experimental conditions in each measurement. The list of GR slit is expressed in horizontal × vertical components.

measurements	0°	forward	finite	elastic
transport mode	disp.	disp.	disp.	achroma.
GR angle (lab.)	0°	2.5°, 4.5°	6°, 9°, 12°	6°, 9°, 12°, 15°
			15°, 18°	18°, 21°, 24°, 27°
				30°, 33°, 36°
GR slit (lab.)	(full open)	(full open)	±20×±30 mr	±20×±30 mr
polarization	-	-	-	0.71
Faraday cup	0 deg.	Q1	S.C.	S.C.
beam intensity	3-4 nA	6-8 nA	10 nA	6-12 nA

Table 2.6: Results of the consistency check of Faraday cups. Values of [the beam current measured by Faraday cup] / [accumulated BLPs events which were subtracted chance events] were listed. Percentages in () were a compared value to the S.C. Faraday cup result.

	0° F.C.	Q1 F.C.	S.C.F.C.
blank target	0.237 (+2 %)	0.233 (+0.4 %)	0.232
target in	0.240 (+3.4 %) ^{58}Ni (4.0 mg/cm^2)	0.235 (+1.3 %) ^{12}C (30 mg/cm^2)	-

Chapter 3

Data Analysis

Several procedures for reconstructing spectra from the experimental data produced by the detector systems were performed with a program code " Tamii Analyzer" [25], which was designed for analyzing the experimental data of the GR and the LAS at RCNP.

3.1 Particle identification

The charge information from the PMTs was used to identify the particle which triggered the event. The energy loss of a charged particle passing through material depends on its charge and velocity by the Bethe-Bloch formula [26]. The light intensity is deexponentially proportional to the energy loss. The intensity is attenuated by the transmission of the photon in the material of the scintillator. The light intensity at the x position is given by

$$I(x) = I_0 \ \exp\Big(-\frac{x}{l}\Big), \tag{3.1}$$

where I_0 is the light intensity where the particle passes, and l is the attenuation length of the plastic scintillator. The geometrical mean I_m of the light outputs from both sides of the scintillation counter is

$$I_m \equiv \sqrt{I(x)I(L-x)} = I_0 \ \exp\Big(-\frac{L}{2l}\Big), \tag{3.2}$$

where L is the length of the plastic scintillator. As an example, values of I_m of the GR PS1 were plotted in Fig. 3.1 for (p, p') scattering at 0°. A wide gate was set for protons from 180 to 600 channels. Similar wide gates to select protons were applied to other spectra of the PSs of the GR and the LAS.

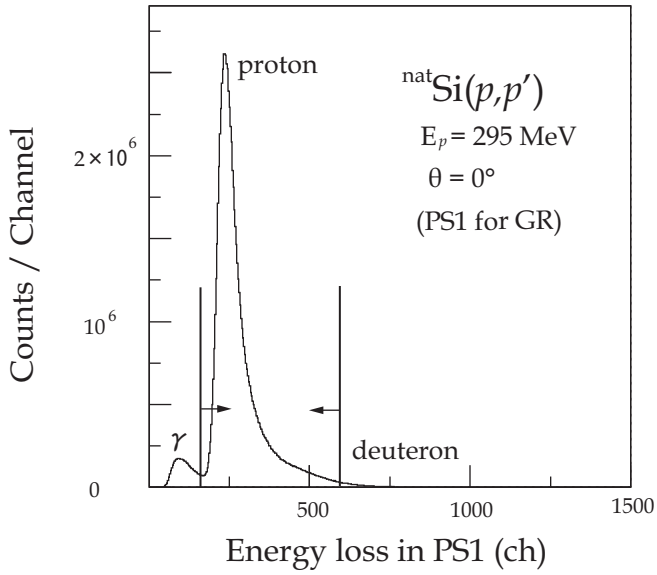

Figure 3.1: Energy loss in the PS1 of the GR in the ^{28}Si(p, p') reaction at 0° deduced by the square root of the product of the charge outputs from the PMTs on both sides. A gate for proton events was set in a range of 180-600 channels as shown in the figure. Deuteron events were not seen.

3.2 Track reconstruction

The structure of each VDC is illustrated in Fig.2.7. When a charged particle passes through the VDC, electron-ion pairs are created along the trajectory. The electrons move to an anode wire in the normal direction to the cathode planes by the force of the electric field. The velocity has an almost constant value of $\sim$ 5 cm/μ sec. The electrons are multiplied at the place close to the anode wire, and generate a negative signal at the anode wire. Usually particles pass through the VDCs in the 45° direction and hit 3 or 4 sense wires.

The vertical drift lengths of d_{i-1}, d_i, ... (Fig. 2.7) were determined from the drift times and gave a particle position at the anode wire plane. The drift lengths were calibrated by a white spectrum which was an uniform distribution of the scattered protons. The drift length histogram should have a flat distribution in a range of 0-10 mm. The conversion tables from the drift time to the drift length have been created from the white spectrum so that the drift length histogram has a flat distribution (Fig. 3.2).

The adjacent hit wires were grouped as a cluster. The intercept position of a trajectory at a wire plane was calculated by a least-square fit method from the drift lengths of the

hit wires in the cluster. By combining the deduced positions at the four wire planes, the trajectory was uniquely determined. The following rules were applied in the determination of trajectories.

- A cluster had at least two hit wires. A single hit wire was not considered as a cluster and was ignored.
- The distribution of the drift lengths in a cluster had only one local minimum which was not at the edge of the cluster.
- The shortest drift time is also used for the ray tracking.
- Least squares fit is performed for all the combination of the multi clusters.
- The number of clusters in each plane was one.

The position resolution was about 0.29 mm in FWHM. The angular resolution was $\tan^{-1}(0.29/250) = 0.066^{\circ}$, which corresponded to a horizontal scattering angle resolution of 0.028° at the target. Here, the value of 250 mm was the distance between VDC1 and VDC2 of the GR.

3.3 Scattering angle calibration

In this section the procedure of deducing the function to reconstruct θ_{tgt} and ϕ_{tgt} is mentioned. The purpose for obtaining the reconstructing function was described in Sec. 2.9.

3.3.1 Obtaining the information of sieve-slit images

For the ray-trace, elastic scattering events were selected using wide gate in x_{fp} one-dimensional histogram (Fig. 3.3) and were plotted in the θ_{fp}-y_{fp} plane (in the left panels of Fig. 3.4). The horizontal position dependence (x_{fp}-dependence) was seen obviously. A gate to select spot images along the y_{fp} direction in the θ_{fp}-y_{fp} plane was applied owing to good separations of the hole images in the θ_{fp} direction. The data gated with θ_{fp} were projected to the y_{fp} axis and a simple Gaussian fit was applied to obtain central y_{fp}

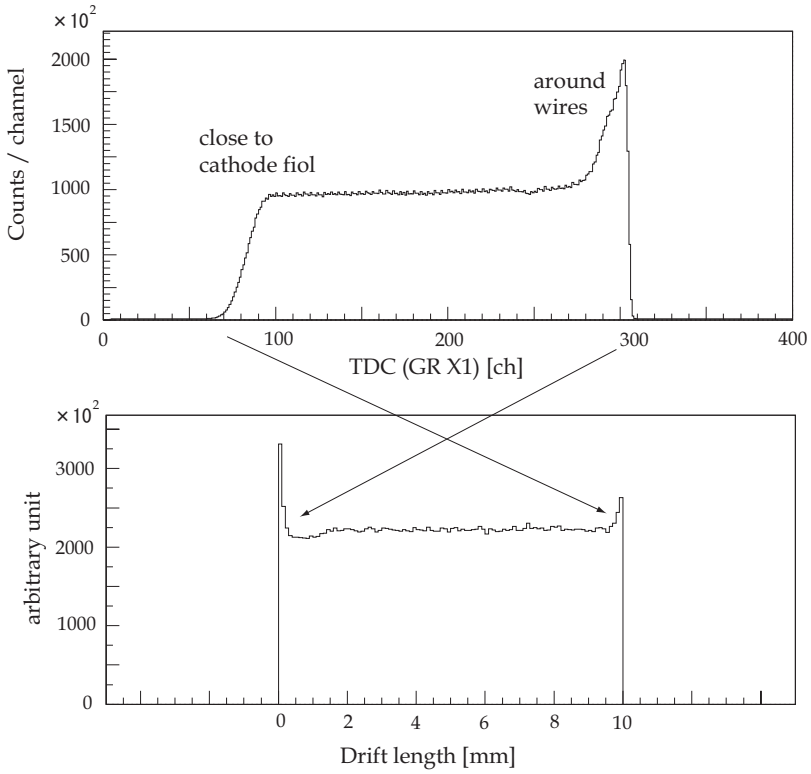

Figure 3.2: Conversion from drift times to drift lengths for the track reconstruction with the VDC. The GR X1 histograms are shown as an example.

values of each peak. It was believed that shapes of hole image were just round. A 5mm thickness of the sieve-slit was so thin that we neglected the influence of the slit thickness.

Next, hole images were sliced by y_{fp} and each was projected to the θ_{fp} axis. Central value of θ_{fp} was obtained for each peak by using a Gaussian function fit. Then, we obtained sets of θ_{fp}, y_{fp} and x_{fp} which were the information of hole positions at the detector plane. Note that data of ten spots at $\theta_{fp} = -1.6$ and -1.1 deg. in Fig. 3.4 (C) were not used for the scattering angle calibration because of difficulties in separating them in the y_{fp} direction.

3.3.2 Study of the suitable function to reconstruct scattering angle

As a next step, suitable function to reconstruct θ_{tgt} and ϕ_{tgt} was studied. The function should be a polynomial expression consisting of θ_{fp}, y_{fp} and x_{fp} and should deduce adequate values of θ_{tgt} and ϕ_{tgt} as well as being simple. From GNU science library function

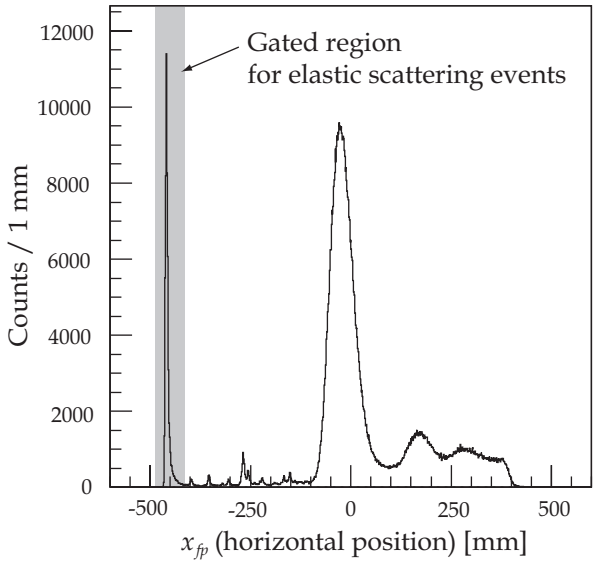

Figure 3.3: A rough gate for selecting elastic scattering events is shown as the shaded area in x_{fp} one-dimensional histogram. The histogram is +1% magnet field parameter data (see Sec. 2.9 for details). Elastic scattering events which lost their energy in the sieve-slit by $\sim$ 10 MeV are seen as the big bump around $x_{fp} = 0$ mm in this figure.

[27], multi-dimensional nonlinear least-squares fitting function[1] was used in order to deduce a suitable reconstructing function. This fitting function evaluated chi-square values per degree of freedom of several functions with different combinations of variables. We chose the following function which gave the minimum chi-square value :

$$\theta_{tgt}(x_{fp}, \theta_{fp}, y_{fp}) = \sum_{i=0}^{2}\sum_{j=0}^{1}\sum_{k=0}^{2} a_{ijk} \cdot {x_{fp}}^i {\theta_{fp}}^j {y_{fp}}^k \tag{3.3}$$

$$\phi_{tgt}(x_{fp}, \theta_{fp}, y_{fp}) = \sum_{i=0}^{2}\sum_{j=0}^{2}\sum_{k=0}^{1} b_{ijk} \cdot {x_{fp}}^i {\theta_{fp}}^j {y_{fp}}^k. \tag{3.4}$$

Here a_{ijk} and b_{ijk} were coefficients of each term and their actual numbers are summarized in Table 3.1. Using ion-optical function which were determined by the fitting function, the horizontal scattering angle resolution of 0.15° and the vertical one of 0.5−0.8° were achieved, that is, the total scattering angle resolution of 0.5° (0.8°) was achieved at E_x = 6 MeV (20 MeV) in FWHM. Reconstructed images of the sieve-slit had similar geometric shape to the original one. They are shown in the right panels of Fig. 3.4.

[1] Original fitting function was modified for the present study by A. Tamii.

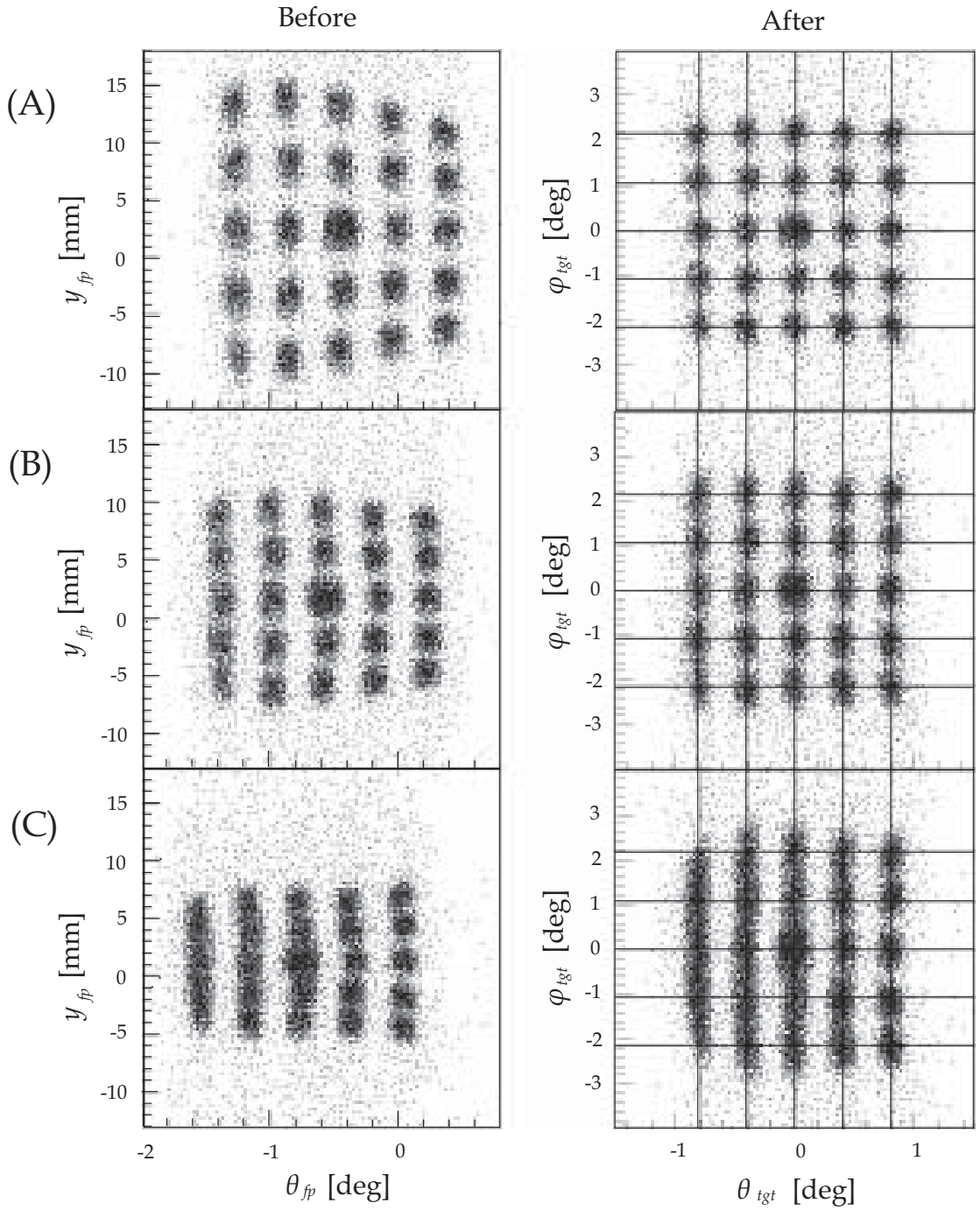

Figure 3.4: Two-dimensional histograms of before (θ_{fp}-y_{fp} plane) and after (θ_{tgt}-ϕ_{tgt} plane) the calibration by software. Images (A), (B) and (C) are taken at the positions corresponding to 6, 13 and 20 MeV of the excitation energy in the magnetic field of the 0° measurement, respectively. Intersections of lines in images of after the calibration are actual hole positions of the sieve-slit. The center of each event in images should coincide with intersections by the calibration.

Table 3.1: Table of coefficients of functions to reconstruct θ_{tgt} and ϕ_{tgt} in radian unit, rightward and upward are positive viewing from upstream, respectively. Numbers of " i, j and k" represents the dimension of x_{fp}, θ_{fp} and y_{fp}, respectively. Here, x_{fp} : horizontal position against for the central ray vertically. The center of VDC is zero and leftward is positive in the view from upstream. θ_{fp} : horizontal angle with respect to the central ray [rad] and leftward is positive. y_{fp} : vertical position from the mid-plane [mm] and upward is positive. See in Sec. 3.3.3 about the bottom column of b_{ijk}.

ijk	a_{ijk}	ijk	b_{ijk}
000	1.490E-02	000	-8.968E-03
010	-4.230E-01	001	5.875E-03
001	-1.475E-05	010	1.653E-02
011	2.984E-04	011	-3.426E-03
002	1.310E-05	020	-1.406E-01
012	-5.372E-05	021	1.069E-01
100	2.610E-05	100	6.294E-06
110	-2.284E-05	101	8.752E-07
101	4.354E-08	110	-5.269E-04
111	-2.379E-06	111	3.058E-04
102	7.077E-09	120	5.764E-03
112	6.123E-07	121	-3.226E-03
200	7.024E-09	200	1.235E-08
210	7.291E-09	201	-8.102E-09
201	1.102E-10	210	-1.021E-06
211	-4.428E-09	211	5.747E-07
202	-2.904E-11	220	1.173E-05
212	1.097E-09	221	-5.996E-06
-	-	000	-(y_{LAS}*0.1804-0.76)*π/180)

3.3.3 Correction of beam position in the vertical direction

Because ion-optical function parameters for the vertical scattering angle were very sensitive to the vertical beam position at the target, the vertical beam position was continuously monitored by the LAS. Fifteen data were taken with the beam spot swung to different points at the target as described in Sec. 2.9. The relation between their false shift of the central hole (ϕ_{sifted}) and vertical position at the focal plane of the LAS (y_{LAS}) was shown in Fig. 3.5. The linearity was obvious and the relation of them was described as $\phi_{shifted} = 0.1924 * y_{LAS} - 0.1786$. Here $\phi_{shifted}$ was described in deg. and y_{LAS} in mm. This means that there was a real correlation between $\phi_{shifted}$ and y_{LAS} due to the experimental setup. The correlation was calibrated and was added in Fig. 3.5 by dotted line. The relation of $\phi_{shifted}$ and y_{LAS} was corrected by adding an term :

$$\phi = -(0.1802 * y_{LAS} - 0.7600). \tag{3.5}$$

The relation was inserted to the function of ϕ_{tgt} as the correctional term of the beam spot position.

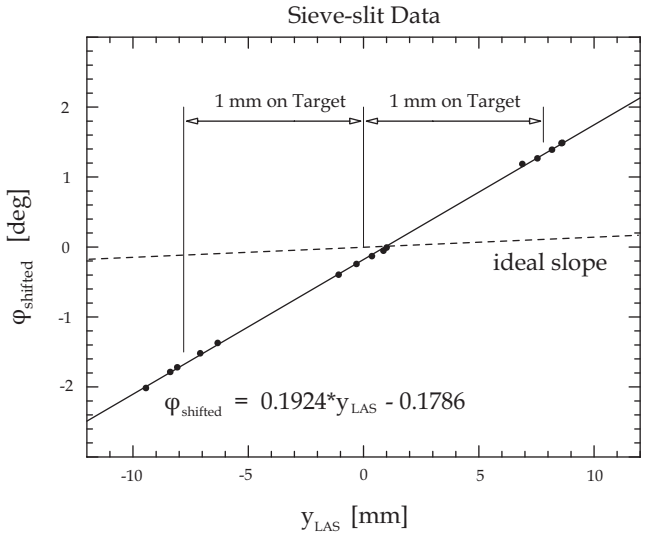

Figure 3.5: Sieve-slit data taken with various shifted beam spots on the target; vertically : -1, 0, 1 mm, horizontally : -8, -4, 0, 4, 8 mm. Solid line is the line fitted to the data and dashed line is the ideal line for the beam spot to be shifted by the correction.

3.3.4 Adequacy of the reconstructing function

Since the reconstructing function was determined by measuring elastic scattering data with changing the magnetic field by 1−5% from that of a normal 0° measurement, whether the function worked properly or not was studied under the 0° magnetic field setting using another sieve-slit. The noticeable point of the new sieve-slit was that the thickness was 15 mm, where the previous one was 5 mm. The energy loss of 295 MeV protons in a 15 mm thickness plate made of brass was sufficient to bend penetrated protons away from the focal plane of the GR. Then we could perform sieve-slit measurements under the 0° magnetic field setting. A thick target of 3 mm plastic scintillator was used for higher statistics since inelastic scattering events were measured. The data were gated at several points of x_{fp} with a 100 mm interval of and were reconstructed. Comparing with actual positions in the θ_{tgt}-ϕ_{tgt} plane, deviations were less than 15% of the angle resolution in both components. It was a sufficient angle resolution for the present study.

The data measured with the thick sieve-slit were not used for determining reconstructing functions because an effect of the thickness on the solid angle of each hole was not negligible. It seems that a simple Gaussian function was not suitable to obtain the information of hole image positions in the θ_{fp}-y_{fp} plane.

3.4 Calibration of the GR ion-optics and kinematical effect

Because we wish to know momentum of scattered protons, the function x_c to be converted to momentum is determined, which depends on x_{fp}, θ_{fp} and y_{fp}. Two-dimensional histograms of x_{fp}-θ_{fp} and x_{fp}-y_{fp} were shown in Fig. 3.6 and vertical lines in images which corresponded to discrete states were bending or broadening due to the GR ion-optics and the kinematics. Cancellation of the ion-optics and the kinematical effect was essential for reconstructing energy spectra with high resolution. The procedure to straighten and sharpen the curves for high resolution spectra is described in this section.

At first we have to know the distorting information of excited states in two-dimensional images of x_{fp}. The vertical lines in the x_{fp}-θ_{fp} plane were divided to more than ten parts with an equal θ_{fp} interval. The data divided with $\Delta\theta_{fp}$ were projected to the x_{fp}

axis. Discrete state positions were deduced by applying a Gaussian function. In order to straighten the curves using the obtained (x_{fp}, θ_{fp}) information, the multi-dimensional nonlinear least-squares fitting function was used which was mentioned in Sec. 3.3.2. After several trials, the function giving the minimum chi-square value and being simpler was determined as $x_c = \sum_{i=0}^{3}\sum_{j=0}^{4}\alpha_{ij}\cdot {x_{fp}}^i{\theta_{fp}}^j$ where x_c was the correctional function and α_{ij}'s were coefficients. The x_{fp} position at $\theta_{tgt} = 0$ was the standard point and was not to be shifted during the correction.

Since ϕ_{tgt} corresponded to the y_{fp} in the present study using the under-focus mode, the x_c depended on y_{fp}. The similar procedure described above was done and the information of (x_c, y_{fp}) was obtained after conversion of the x_c from the θ_{fp}. By using the fitting function we obtained the following function :

$$x_c = \sum_{i=0}^{3}\sum_{j=0}^{4}\alpha_{ijk}\cdot {x_{fp}}^i{\theta_{fp}}^j + \sum_{i=0}^{3}\sum_{k=0}^{2}\beta_{ijk}\cdot {x_{fp}}^i{y_{fp}}^k \tag{3.6}$$

with keeping x_c ($\theta_{tgt} = \phi_{tgt} = 0$) = x_{fp} ($\theta_{tgt} = \phi_{tgt} = 0$). Despite of performing the iteration twice, the curves of discrete states in the x_c-θ_{tgt} image were still twisty. The iteration was again performed using the (x_c, θ_{fp}) information. The straightened and sharpened lines were finally achieved as shown in the x_{fp}-θ_{tgt} plane of Fig. 3.7 and in the x_{fp}-ϕ_{tgt} plane of Fig. 3.8. With the corrections, we achieved an energy resolution of 20 keV for the 295 MeV ^{28}Si(p, p') experiment after background subtraction and after a scattering angle cut of $0.0-0.5^\circ$.[2] This was an amazing accomplishment comparing with the previous one, 150 keV [28]. The same calibration procedure was applied to all the forward angles data to reconstruct energy spectra with high resolution.

3.5 Background subtraction

Although we succeeded in reducing the background arising from the beam-halo, background still remained resulting mainly from multiple scatterings of the beam on the target. The procedure of the subtraction of background events from the excitation energy spectra is described in this section.

[2]One of the best energy resolution was 17 keV achieved at $E_x = 11.45$ MeV state.

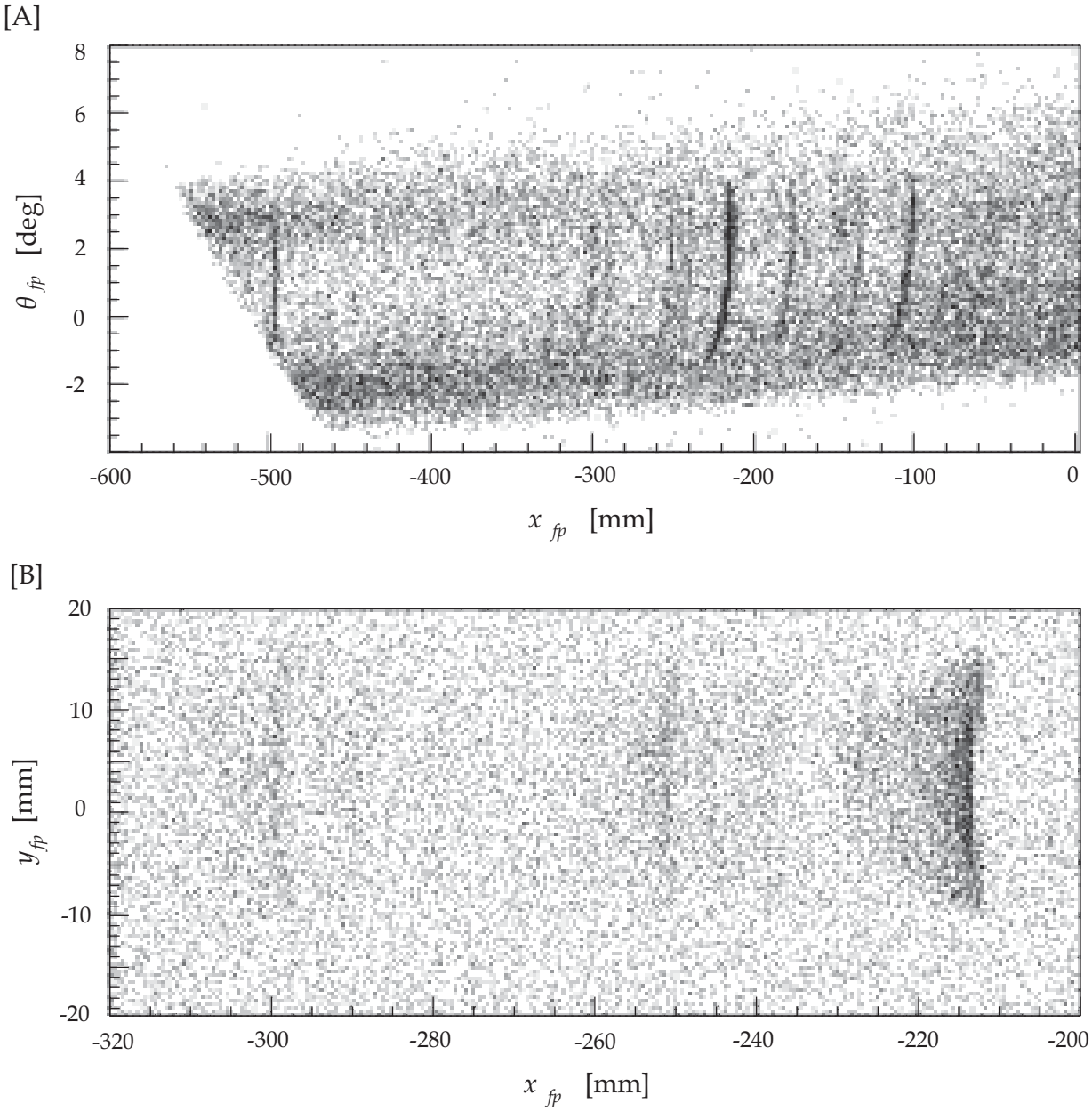

Figure 3.6: Two-dimensional histograms of [A] x_{fp}-θ_{fp} and [B] x_{fp}-y_{fp} for ^{28}Si(p, p') at 0° before correction. [A] : The acceptance around $x_{fp} = -500$ mm is suffered from the lead block for reducing background events. The vertical lines which corresponds to excited states are vending by the influence of ion-optics. [B] : The vertical lines seen broad should be sharpened for a high resolution energy spectrum.

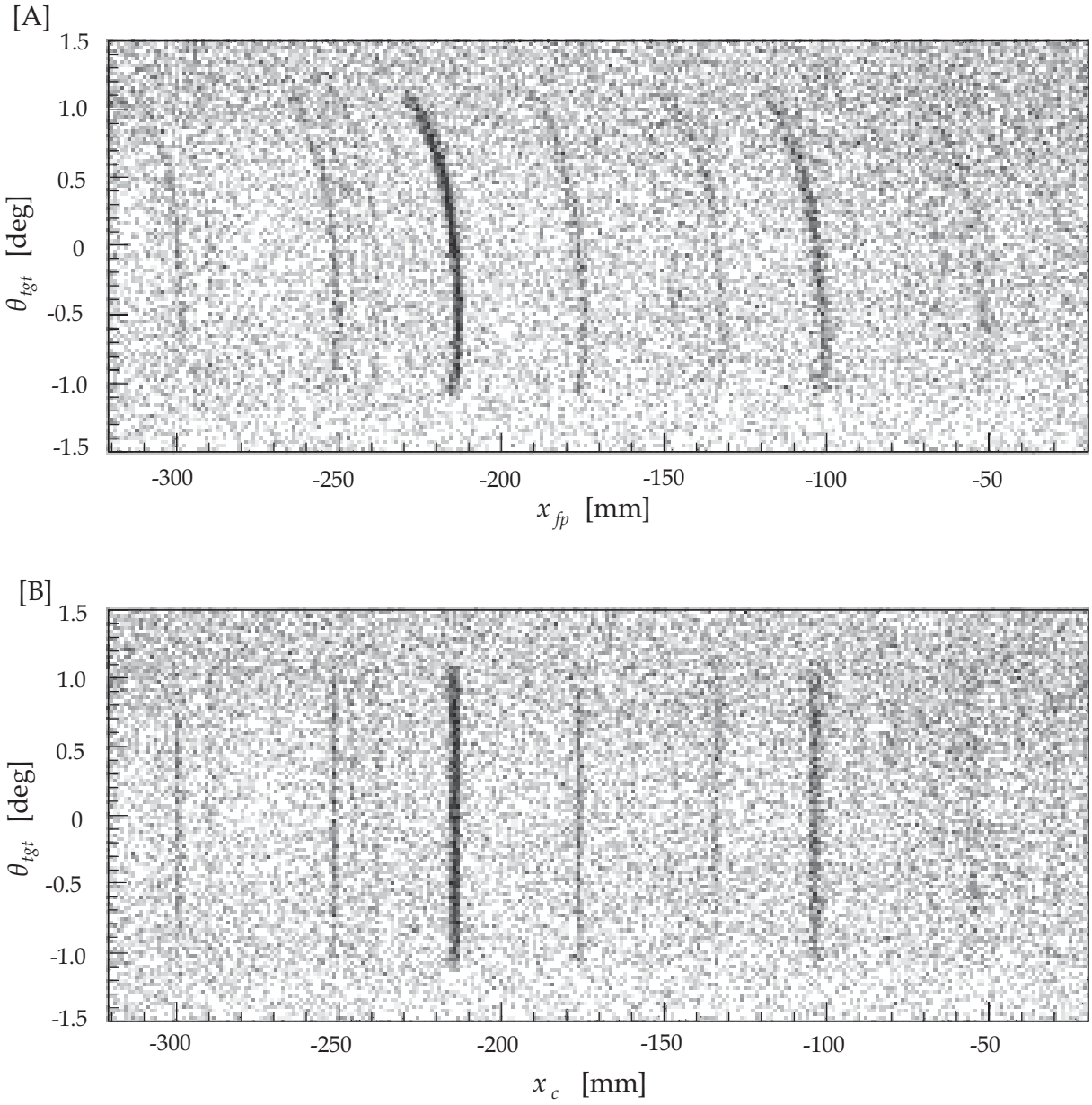

Figure 3.7: Two-dimensional histograms of x_{fp}-θ_{tgt} [A] without and [B] with correction. [A] : The ion-optical property of the GR creates the curve of the loci which correspond to excitation of discrete states. [B] : The aberrations of x_{fp} for the θ_{tgt} are corrected by software and excited states are straightened.

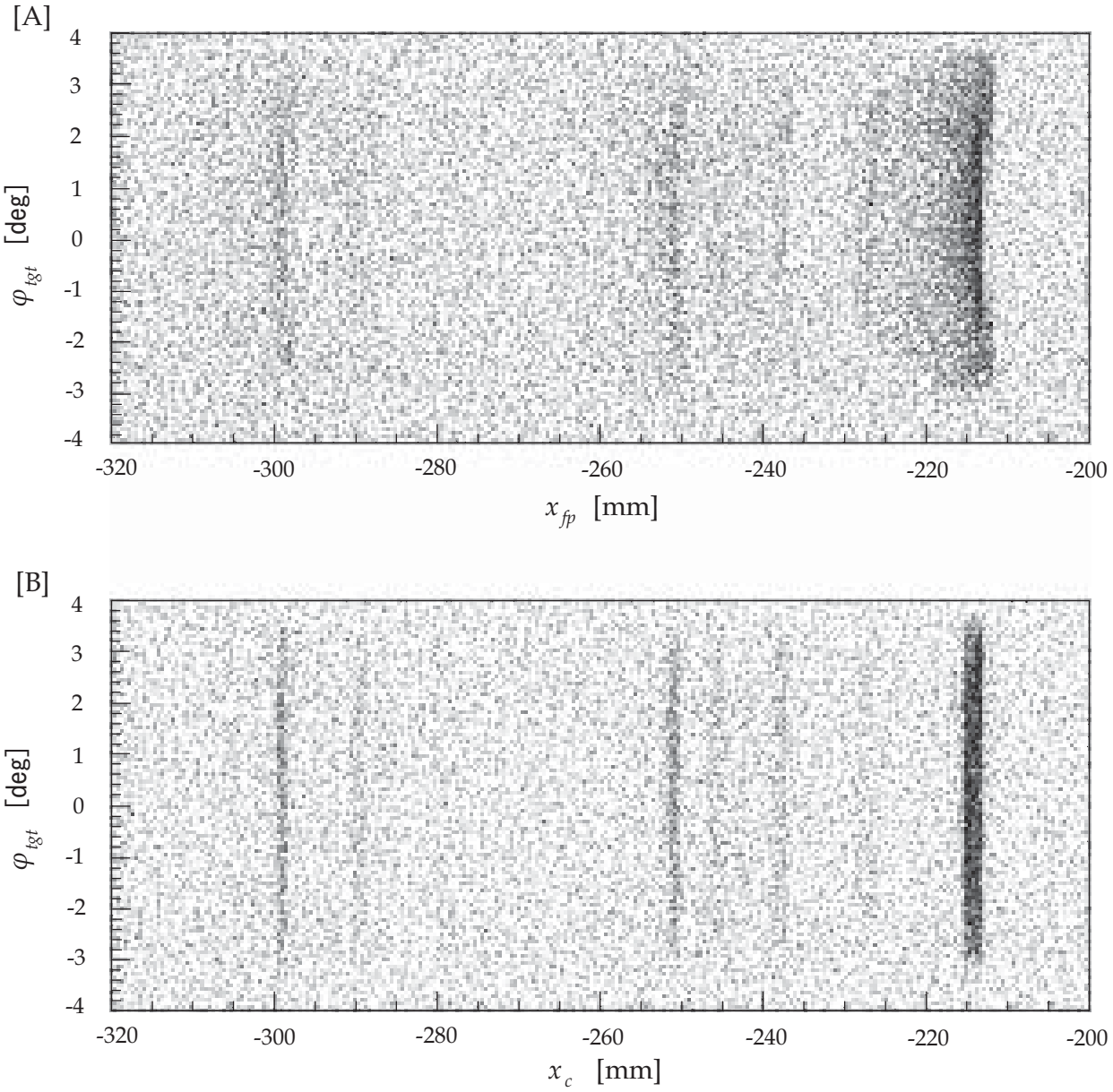

Figure 3.8: Two-dimensional histograms of x_{fp}-ϕ_{tgt} [A] without and [B] with correction. [A] : The ion-optical property of the GR creates the curve of the loci which correspond to excitation of discrete states. [B] : The aberrations of x_{fp} for the ϕ_{tgt} are corrected by software and excited states are sharpened.

3.5.1 Focusing in the vertical direction

Background events due to the multiple scattering at the target and re-scattering in the spectrometer had a flat distribution in the histogram of the vertical (y) position at the focal plane. In contrast, from the original ion-optical feature of the GR spectrometer, true events, *i.e.* inelastically scattered protons, were focused at the focal plane not only in the horizontal direction but also in the vertical direction. However focusing in the vertical direction was not performed in the present experiment owing to the under-focus mode. Focusing true events in the vertical direction by software was essential for distinguishing true events from background ones. Obtained data plotted in the two-dimensional histogram of the y_{fp}-ϕ_{fp} were shown in Fig. 3.9 [A]. The y_{fp}-ϕ_{fp} relation had an x_{fp} dependence. The histograms in Fig. 3.9 were created by selecting the $E_x = 11.45$ MeV state for ^{28}Si(p, p') at 0°. In the image of Fig. 3.9 [A], true events leaned by de-focusing in the vertical direction at the detector plane while background events were scattered. Since the projection of the true events on the y_{fp} axis was a broad peak as seen in Fig. 3.9 [C], distinguishing background using distribution of the vertical position was not efficient. Then we rotated[3] true events in order to stand them up in the y_{fp}-ϕ_{fp} plane and we adjusted them to be along $y = 0$ using the beam spot position information of y_{LAS} measured by the LAS (Fig. 3.9 [B]). The former operation corresponded to focusing true events in the vertical direction, which stood a sharp peak consisting of true events in one-dimensional y_c histogram (Fig. 3.9 [D]). The latter one was done in order to handle all data in a consistent manner because 8 runs of the 0° measurement were taken. The operation was performed by the function which was deduced by multi-dimensional nonlinear least-squares fitting function as the following :

$$y_c = \Big(\sum_{i=0}^{3} \sum_{j=0}^{1} \kappa_{ij} \cdot {x_{fp}}^i {\phi_{fp}}^j + y_{fp} \Big) + \sum_{k=0}^{2} \sum_{l=0}^{1} \lambda_{kl} \cdot {x_{fp}}^k {y_{LAS}}^l. \tag{3.7}$$

Here y_c was the correction function and κ_{ij} and λ_{kl} were coefficients for each term. The part surrounded by () in the equation corresponded to the former operation which was a kind of rotation. The actual number of the coefficients, κ_{ij} and λ_{kl}, are summarized in Table 3.2.

[3]The operation was not a rotation in a strict sense.

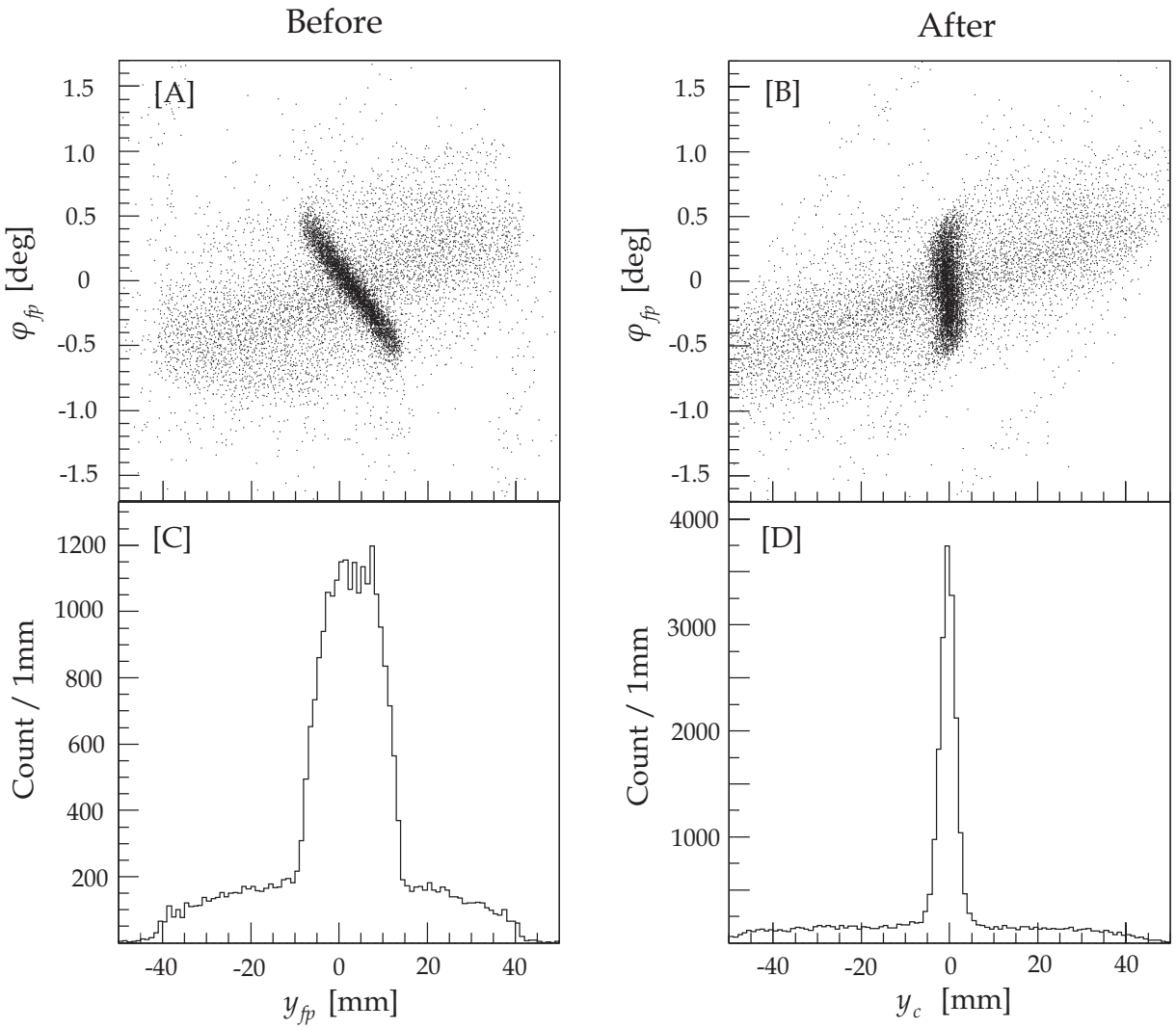

Figure 3.9: Two-dimensional histogram of the y_{fp}-ϕ_{fp} plane with a gate selecting E_x = 11.45 MeV state for ^{28}Si(p, p') at 0° before ([A], [C]) and after ([B], [D]) correction. [A] : True events are leaned due to de-focusing in the vertical direction at the detector plane and background events are scattered. [B] : True events has been rotated and shifted to be along $y = 0$ using the correctional function. [C] : Projected to the y_{fp} axis before correction. [D] : Projected to the y_{fp} axis after correction. A sharp peak consisting of true events and a flat distribution of background events are seen.

Table 3.2: Table of coefficients of functions for focusing in the vertical direction and shifting to the axis $y_c = 0$ in mm unit, rightward and upward are positive viewing from upstream, respectively. Numbers of " i, j" represents the dimension of x_{fp} and ϕ_{fp}, respectively. Here, x_{fp} : horizontal position against for the central ray vertically. The center of VDC is zero and leftward is positive in the view from upstream. ϕ_{fp} : vertical angle with respect to the central ray [rad] and upward is positive. Numbers of " k, l" represents the dimension of x_{fp} and y_{LAS}, respectively. y_{LAS} : vertical position of the LAS in mm.

ij	κ_{ij}	kl	λ_{kl}
00	-2.309E-00	00	1.392E-00
01	9.525E+02	10	-1.204E-03
10	-6.549E-04	20	1.527E-06
11	-1.493E-00	01	-8.064E-01
20	-5.226E-07	11	5.826E-04
21	1.528E-03	21	-5.677E-07
30	1.007E-06		
31	-1.962E-06		

3.5.2 Background subtraction

In the conventional analysis of full-acceptance data of the GR, a gate with the y_c which width depended on the x_{fp} is applied to select true events including background ones. In order to subtract background events from them, a uniform background distribution is assumed. Gates, the width of which is the same as that for selecting true events, are applied to both side of the sharp peak in the y_c one-dimensional histogram. We assume that the average of both selected background events corresponds to those of the bottom of sharp peak in the true gate.

The technique mentioned above, however, is used for handling full-acceptance data. Since we intended to use the data applied a scattering angle cut for better angle resolution, the special operation was done as the following : we artificially shifted the y_{fp}-ϕ_{fp} image along the scattered direction of background events before any corrections, and then applied exactly the same analysis procedure including gates as well as the correction to focus true events in the vertical direction. The scattered direction was common at any x_{fp} position because of a flat distribution of background events although the distance of shifting the image in the y_{fp}-ϕ_{fp} plane had an x_{fp} position dependence. After shifting the image in the y_{fp}-ϕ_{fp} plane to the upward and the downward, the same analysis procedure in the

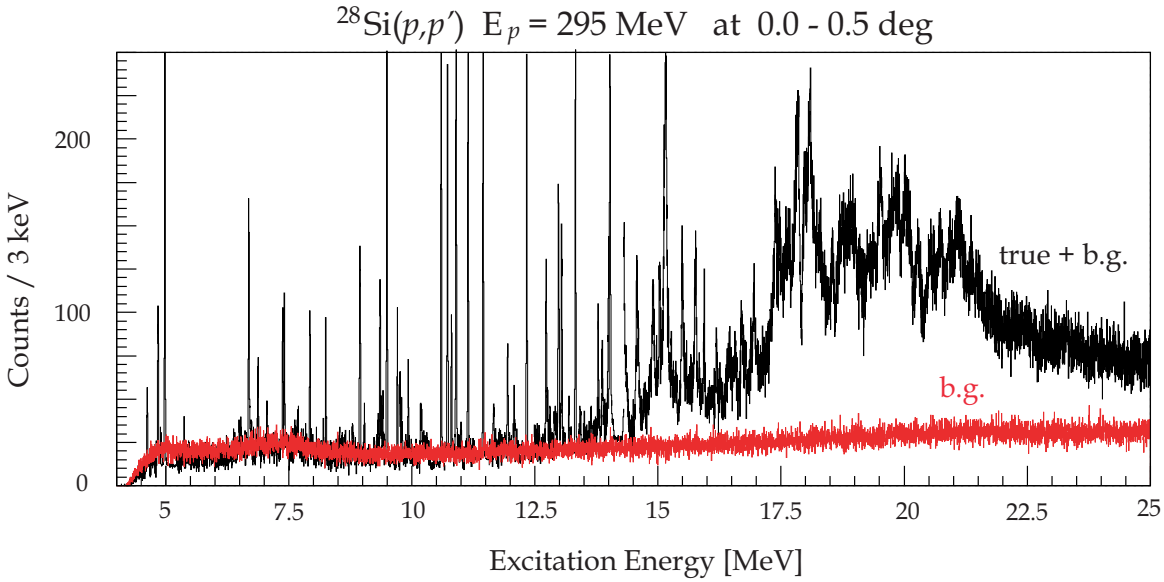

Figure 3.10: Excitation energy spectrum and background one for the ^{28}Si(p, p') reaction at 0.0−0.5°. True events including background with a scattering angle gate of 0.0−0.5° are drawn by the black spectrum. The average of background events gated in 0.0−0.5° obtained by artificially shifting the events to the upward and the downward along the scattered direction in the y_{fp}-ϕ_{fp} plane are drawn by the red one. Background subtraction appears working reasonably because of a flat distribution of the red spectrum. Note that the disagreement between true + $b.g.$ and $b.g.$ around $E_x = 5$ MeV is due to an insufficient acceptance as shown in the top panel of Fig. 3.6.

case of full-acceptance analysis was performed. Since the red spectrum in Fig. 3.10 which corresponded to the average of estimated background events well reproduces a continuum line at discrete state, background subtraction looked working reasonably.

3.6 Energy calibration

In a magnetic field, a bounding radius of charged particle depends on the momentum as the following equation :

$$B\rho = \frac{p}{q_c}, \tag{3.8}$$

where B is the magnetic field of the spectrometer, ρ is the radius of the orbit, p is the momentum and q_c is the charge of the particle. Because of the linearity between the momentum (p) and the radius of the mean orbit (ρ) in the GR, inelastically scattered protons detected at a x_{fp} was proportional to a momentum of itself. Since the kinematical energy of a particle was proportional to the square of the momentum within non-relativistic, the square of x_{fp} was converted to the excitation energy. Using this relation between the x_{fp} and the excitation energy, the energy scale was determined by being fitted to the well-known excited states as a quadratic function of x_{fp} [7, 8].

3.7 Elastic scattering

In this section derivation of elastic scattering data is described.[4] The beam polarization of upward ($p_\uparrow$) and downward ($p_\downarrow$) was assumed as $p_\uparrow = -p_\downarrow$ in the present analysis.

3.7.1 Beam polarization

The beam polarization was measured by BLP consisting of four scintillation telescopes in two pairs at conjugate angles as mentioned in Sec. 2.6. Beam polarization p was given by

$$p = \frac{1}{A_y^{BLP}} \frac{L-R}{L+R} \tag{3.9}$$

where L and R were measured yields at left and right scatterings, respectively, and A_y^{BLP} was the analyzing power of pp elastic scattering at 17° in laboratory frame. A_y^{BLP} was

[4] Ref. [29] was refered mainly.

measured by previous experiments as 0.40 ± 0.01 for 300 MeV incident protons [30]. As mentioned in Sec. 2.1.2, the beam polarization was cycled between spin-up (↑) and spin-down (↓) and measured yields of left and right detectors for the spin state were described as $L_\uparrow$, $R_\uparrow$, $L_\downarrow$ and $R_\downarrow$. The beam polarization was described as followings :

$$p_\uparrow = \frac{1}{A_y^{BLP}} \frac{L_\uparrow - R_\uparrow}{L_\uparrow + R_\uparrow} = \frac{1}{A_y^{BLP}} \frac{1 - R_\uparrow/L_\uparrow}{1 + R_\uparrow/L_\uparrow} \tag{3.10}$$

$$p_\downarrow = \frac{1}{A_y^{BLP}} \frac{L_\downarrow - R_\downarrow}{L_\downarrow + R_\downarrow} = \frac{1}{A_y^{BLP}} \frac{1 - R_\downarrow/L_\downarrow}{1 + R_\downarrow/L_\downarrow}. \tag{3.11}$$

Since $p_\uparrow = -p_\downarrow$ was assumed, the beam polarization and its statically error were given by

$$p = \frac{1}{A_y^{BLP}} \frac{1-x}{1+x} \tag{3.12}$$

$$\Delta p = \frac{1}{A_y^{BLP}} \frac{x}{(x+1)^2} \sqrt{\left(\frac{(x+1)^2}{x} p_y \Delta A_y^{BLP} \right)^2 + \left(\frac{1}{L_\uparrow} + \frac{1}{L_\downarrow} + \frac{1}{R_\uparrow} + \frac{1}{R_\downarrow} \right)}, \tag{3.13}$$

where

$$x \equiv \sqrt{\frac{R_\uparrow L_\downarrow}{L_\uparrow R_\downarrow}} \tag{3.14}$$

using following relation :

$$\frac{R_\uparrow}{L_\uparrow} = \left(\frac{R_\downarrow}{L_\downarrow} \right)^{-1} = \frac{L_\downarrow}{R_\downarrow}. \tag{3.15}$$

3.7.2 Differential cross section and analyzing power

Measured yields (N) for each spin were given by

$$N_\uparrow = \left(\frac{d\sigma}{d\Omega} \right)_{lab} (1 + p_\uparrow A_y) Q_\uparrow \Omega x \epsilon_\uparrow l_\uparrow \tag{3.16}$$

$$N_\downarrow = \left(\frac{d\sigma}{d\Omega} \right)_{lab} (1 + p_\downarrow A_y) Q_\downarrow \Omega x \epsilon_\downarrow l_\downarrow, \tag{3.17}$$

where $(d\sigma/d\Omega)_{lab}$ was differential cross section of ground state, p was the beam polarization, A was the analyzing power, Q was the quantity of beam, Ω was the solid angle of the GR, x was the number of atomic as the target, ϵ was the efficiency of detectors and l

was the live time of DAQ. From these the differential cross section and analyzing power were deduced as followings :

$$\frac{d\sigma}{d\Omega} = \frac{1}{2}\Big(\frac{N_\uparrow}{Q_\uparrow \epsilon_\uparrow l_\uparrow} + \frac{N_\downarrow}{Q_\downarrow \epsilon_\downarrow l_\downarrow}\Big) \times \frac{1}{\Omega x} \tag{3.18}$$

$$A_y = \frac{1}{p}\frac{\frac{N_\uparrow}{Q_\uparrow \epsilon_\uparrow l_\uparrow} - \frac{N_\downarrow}{Q_\downarrow \epsilon_\downarrow l_\downarrow}}{\frac{N_\uparrow}{Q_\uparrow \epsilon_\uparrow l_\uparrow} + \frac{N_\downarrow}{Q_\downarrow \epsilon_\downarrow l_\downarrow}} \tag{3.19}$$

using the relation of $p_\uparrow = -p_\downarrow$.

Chapter 4

Results

Inelastic scattering data (forward angles data) were used for reconstructing energy spectra. Elastic scattering data were used for obtaining an optical potential of ^{28}Si at E_p = 295 MeV.

4.1 Reduction of cross section

4.1.1 Excitation energy spectra

The excitation energy spectrum for the ^{28}Si(p, p') reaction at E_p = 295 MeV with a scattering angle gate of 0.0−0.5° is shown in Fig. 4.1. Owing to the good scattering angle resolution by under-focus mode, the forward angles data have been separated into a few part. The data measured at $\theta_{lab} = 0°$ are divided into θ_{lab} = 0.0−0.5°, 0.5−1.5° and 1.5−2.5°, which corresponds to θ_{cm} = 0.36°, 1.03° and 1.99°, respectively. Inelastically scattered protons were measured in a broad excitation energy region of 5−25 MeV although an acceptance of the 0^+ state at E_x = 5.00 MeV can be insufficient from the lead block for reducing background events as seen in Fig. 3.6 [A] at $x_{fp} = -500$ mm. The energy resolution of 20 keV in FWHM has been achieved and background subtraction has been performed reasonably. One of the best energy resolution is 17 keV at E_x =11.45 MeV state. We have realized the 0° measurement where $\Delta L = 0$ transitions including $M1$ have the maximum cross section. The high quality spectrum of the present work is compared with a previous one of Crawley *et al.* [8] as shown in Fig. 4.2. Quality of the spectrum has been vastly improved. Note that the incident proton energy is different. Energy spectra at finite angles are shown in Fig. 4.3 together with the spectrum at 0°.

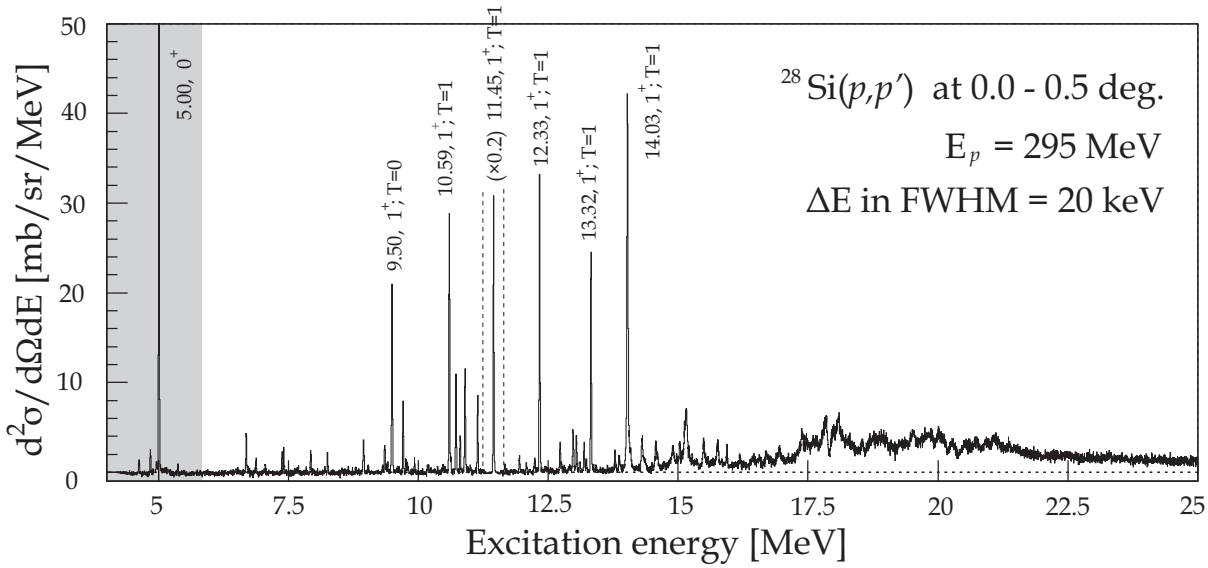

Figure 4.1: An excitation energy spectrum for the ^{28}Si(p, p') reaction at $E_p = 295$ MeV with a scattering angle gate of $0.0-0.5^\circ$ with background subtraction. The acceptance of the shaded region might be insufficient from the beam duct to the 0° dump. An energy resolution of 20 keV in FWHM has been achieved. One of the best energy resolution is 17 keV at E_x =11.45 MeV.

4.1.2 Peak fitting

The yields for peaks are obtained by fitting the energy spectra. Since the spectra are taken with high resolution, peak shapes are well reproduced by using the following function :

$$f(E_x) = a + bE_x + c\exp\left\{ -\left(\frac{E_x - E_0}{d}\right)^2\right\}, \tag{4.1}$$

where E_0 is the central energy and c, d are peak-shape parameters. The symbols a and b are the parameters to reproduce a linear background.

4.1.3 Differential cross section

Differential cross sections for the discrete states have been deduced by the following equation

$$\frac{d^2\sigma}{d\Omega dE} = \alpha N \frac{1}{d\Omega}\frac{1}{L}\frac{1}{\eta}\frac{e}{Q}\frac{A}{N_A t a}J \tag{4.2}$$

The notation of the variables is summarized in Table 4.1. The statistical uncertainty is given by the following equation

$$\Delta\frac{d^2\sigma}{d\Omega dE} = \frac{1}{\sqrt{N}}\frac{d^2\sigma}{d\Omega dE} \tag{4.3}$$

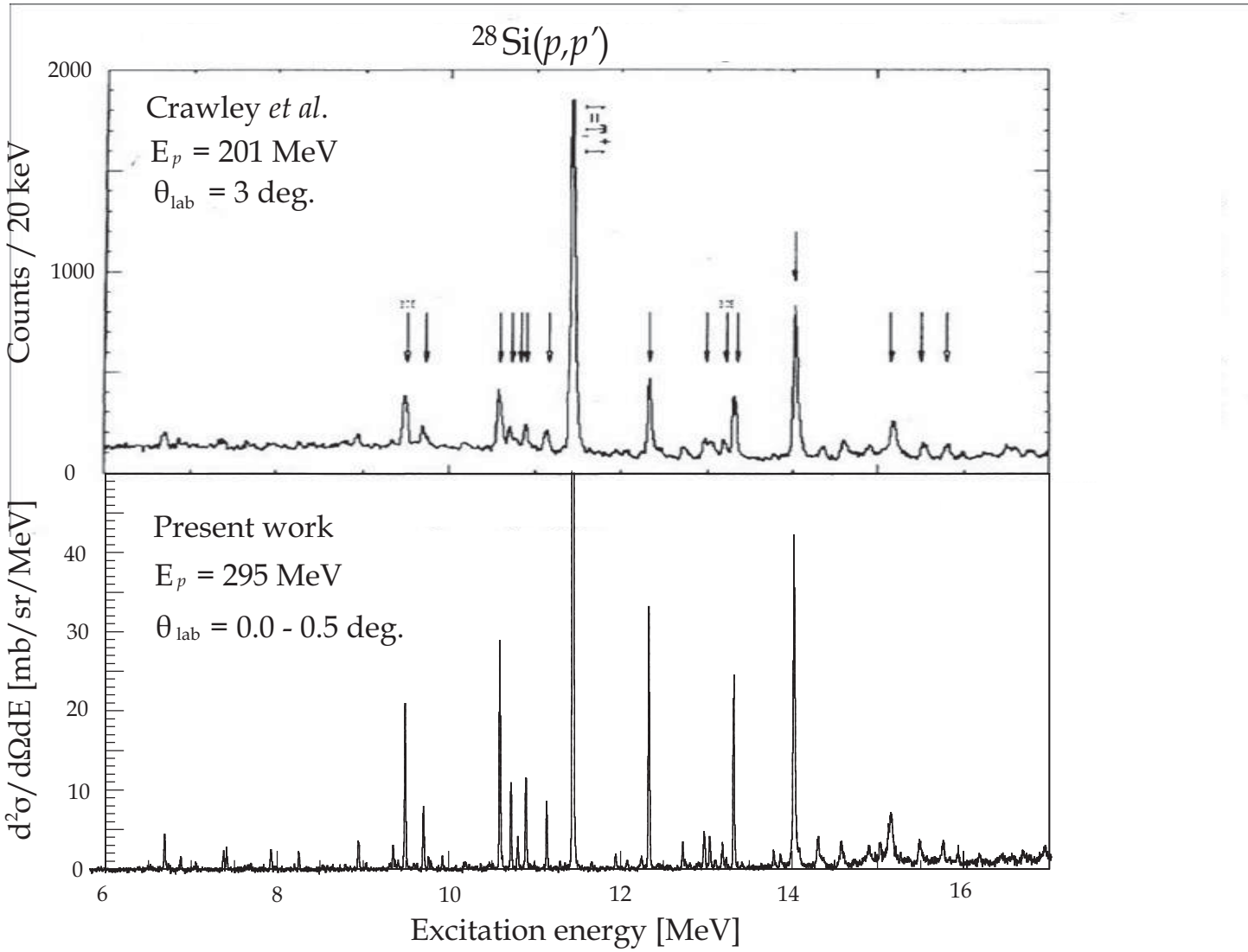

Figure 4.2: An expanded spectrum for discrete states of the ^{28}Si(p, p') reaction at E_p = 295 MeV at 0.0−0.5° of the present work is compared with a previous one of Crawley *et al.* [8] at E_p = 201 MeV at 3°. We have realized the very 0° measurement where $M1$ states have the maximum cross section. Additionally, in the spectrum of the present work, sharper peaks due to better resolution and less background are seen. Note that the incident proton energy is different.

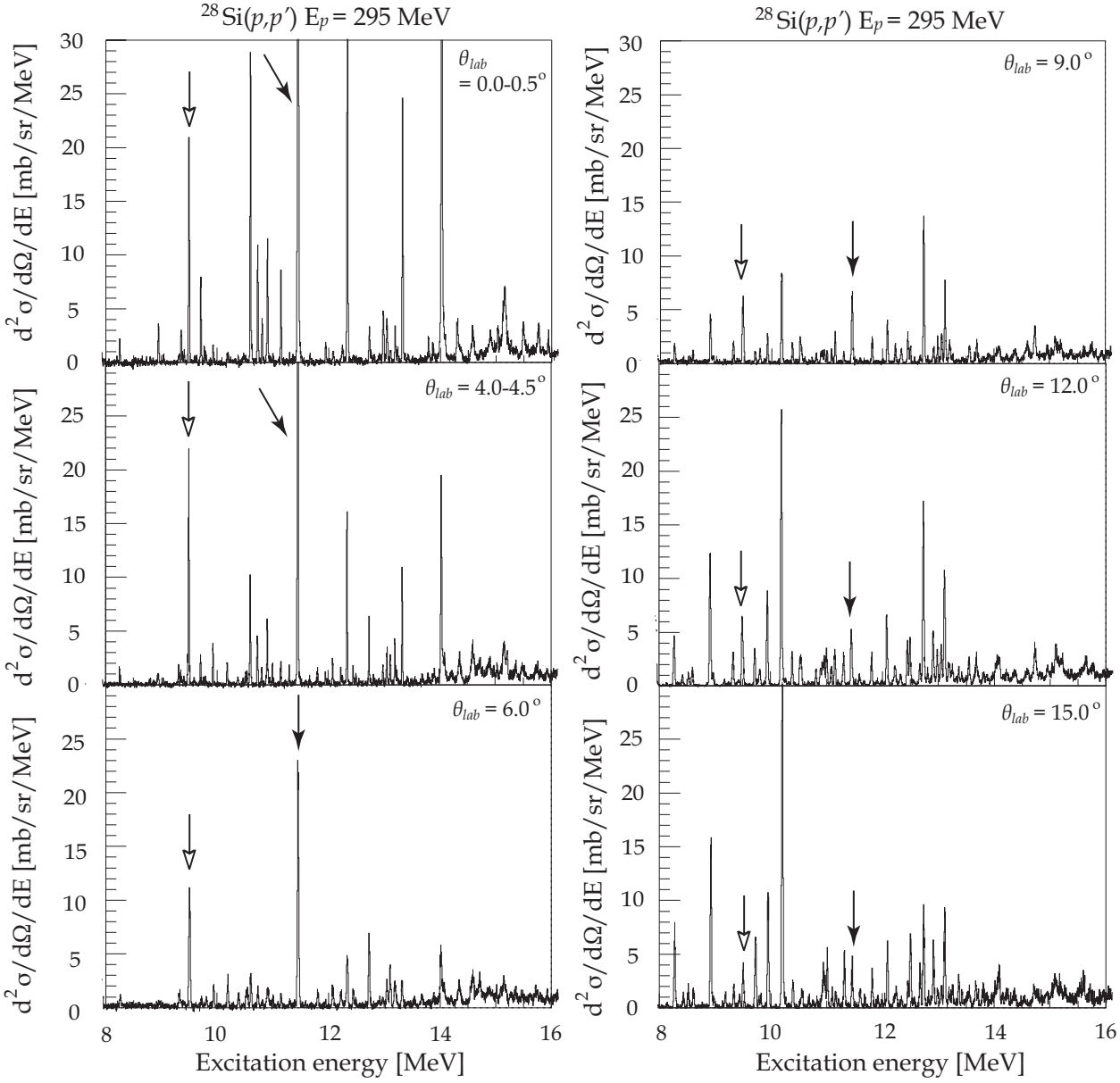

Figure 4.3: Excitation energy spectra for the ^{28}Si(p, p') reaction at $E_p = 295$ MeV at θ_{lab} = 0−15°. The opened arrows indicate the 1^+, $T = 0$ state at $E_x = 9.50$ MeV. The filled arrows indicate the 1^+, $T = 1$ state at $E_x = 11.45$ MeV.

Table 4.1: Notation of the variables used in the expression of the differential cross section in Eq. 4.1 and their values used in the calculation.

$\frac{d^2\sigma}{d\Omega dE}$	double differential cross section		[mb/sr·MeV]
α	unit conversion constant	10^{30}	[mb/cm^2·mg/g]
N	number of detected particles in the energy region between E and $E + \Delta E$		[counts/MeV]
dΩ	solid angle (lab.)		[sr]
L	live time ratio of DAQ		[-]
η	VDC efficiency		[-]
e	elementary charge	1.60×10^{-19}	[C]
Q	integrated beam charge		[C]
A	target atomic weight	28.09	[g/mol]
N_A	Avogadro number	6.02×10^{24}	[mol^{-1}]
t	target thickness		[mg/cm^2]
a	target abundance	92.23	[%]
J	Jacobian from lab. to CM		

4.2 Optical potential

Results of elastic scattering measured by using a polarized beam are described in this section.

4.2.1 Beam polarization

The proton beam polarization has been stable during the elastic scattering experiment as shown in Fig. 4.4. The polarization was stable around 72 %.

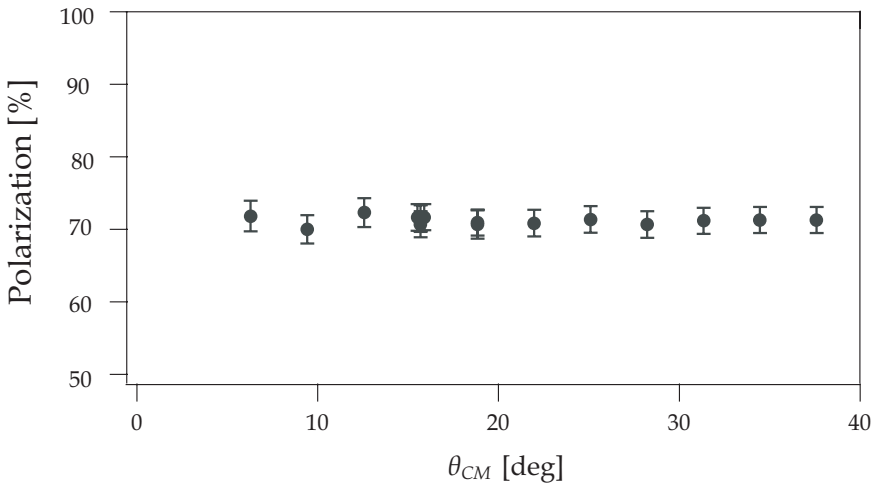

Figure 4.4: The polarization of the beam has been stable around 72 %.

4.2.2 Calibration of target thickness

The thickness of the thin foil target has been calibrated against the wafer target by measuring elastic scattering data at 18° since the thickness of the wafer is reliable due to its homogeneity. The value of the cross section deduced from the foil target data has been normalized to that of the wafer. As a result the thickness of the thin foil target has been determined to be 2.22(2) mg/cm^2 where uncertainty is from the statistics.

4.2.3 Optical potential

An angular distribution of the cross section and the analyzing power for the ^{28}Si(p, p_0) reaction at $E_p = 295$ MeV are shown in Fig. 4.5. A Woods-Saxon (WS) type function has been assumed for the optical potential by the following equation :

$$\begin{aligned} V(r) &= V_{coul} + VF_0(r) + iWF_w(r) \\ &\quad + \Big\{\frac{\hbar}{m_\pi c}\Big\}^2 [V_{so}G_{so}(r) + iW_{so}G_{wso}(r)]\vec{L}\cdot\vec{\sigma}, \end{aligned}$$

where

$$F_k(r) = \Big[1 + \exp\Big(\frac{r - r_k A^{1/3}}{a_k}\Big)\Big]^{-1} \quad k = 0,\ w$$

$$G_k(r) = \frac{1}{r}\frac{d}{dr}\Big[1 + \exp\Big(\frac{r - r_k A^{1/3}}{a_k}\Big)\Big]^{-1} \quad k = so,\ wso.$$

The set of optical potential is taken from Ref. [31], which is summarized in Table 4.2. The V_{coul} is the Coulomb potential of a uniformly charged sphere with the radius $R_c = 1.05$ fm. The result of the DWBA calculation using Table 4.2, which is described in Sec. 5.2, is also drawn by the solid curve in Fig. 4.5. The experimental results are well reproduced by the calculation. The set in Table 4.2 is used for the DWBA in the present study.

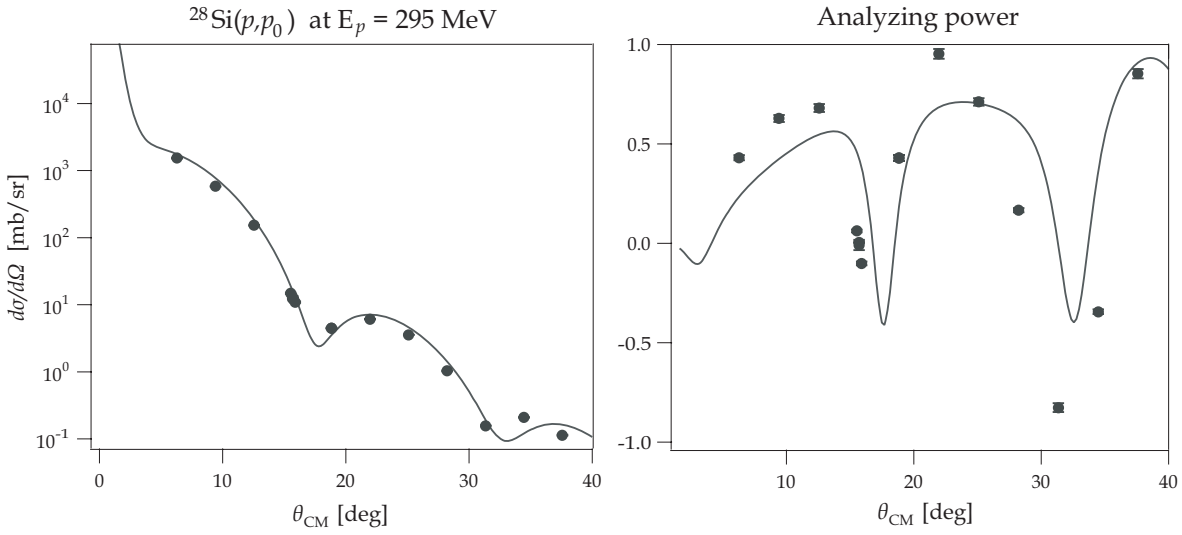

Figure 4.5: An angular distribution of the cross section of elastic scattering events and analyzing power for the ^{28}Si(p, p_0) reaction at $E_p = 295$ MeV. Curves in the histograms are not the best fit but a good fit. The optical potential parameters are summarized in Table 4.2.

Table 4.2: Parameters of the optical potential of ^{28}Si at $E_p = 295$ MeV to be used in DWBA calculations (Energies in MeV, lengths in fm). Taken from Ref. [31].

V_0	r_0	a_0	W	r_w	a_w
-30.9	0.975	0.491	-20.1	1.142	0.659

V_{so}	r_{so}	a_{so}	W_{so}	r_{wso}	a_{wso}
-0.916	1.063	0.747	8.56	1.063	0.747

Chapter 5

Extraction of B(σ) strength

In this chapter, the B(σ) strength is obtained by using the cross section data at very forward angles. Spin-parity assignments as 1^+ and the identification of the isospin are performed by comparing calculated angular distributions with experimental results. The (p, p') cross sections are extrapolated to at zero momentum transfer using DWBA calculations. Finally they are converted to the B(σ) strengths using unit cross sections obtained by calculations.

5.1 Shell model calculation

A shell model calculation is performed by using the code OXBASH [32]. A *sd*-shell model space and an ^{16}O core are assumed in the calculation. It restricts particles and holes in the $1d_{5/2}$, $1d_{3/2}$ and $2s_{1/2}$ single particle orbit. Used effective interactions are two. One is called USD [33] which was deduced from realistic interactions based on the KUO interaction [34]. Another interaction is called KUOSDM[1] (KUOM) which was deduced from a fundamental nuclear force with a modification of the mass dependence, $(A/18)^3$. The shell model calculation is used to derive one body transition densities (OBTDs) and the B(σ) strength distributions. The obtained OBTDs are input to the DWBA calculation which is described in Sec. 5.2.

[1] A mass dependence, $(A/18)^3$, was added to the original interaction " KUO" obtained by T.T.S. Kuo [34]. Note that the interaction KUOSDM is expressed as KUOM in this paper.

5.2 DWBA calculation

The distorted wave impulse approximation (DWIA) calculation is used to calculate a nuclear scattering observable of a one step process due to the direct reaction process within the impulse approximation. The calculation takes account of the distortion effect macroscopically. This is called as the distorted wave Born approximation (DWBA). In the present study, the code DWBA91 [35] is used for performing the DWBA calculations. The effective nucleon-nucleon interaction is taken from the t-matrix parameterization of the free NN interaction by Franey and Love at 325 MeV [36]. The optical potential which describes a distortion for both incoming and outgoing waves is listed in Table 4.2. The OBTDs calculated by OXBASH and the harmonic oscillator size parameter of $b = 1.82$ fm [7] are used.

5.3 J^π and isospin assignments

In order to select $M1$ excitations and to identify the isospin value, measured angular distributions are compared with the DWBA curves. Curves calculated by DWBA for several OBTDs using the USD interaction are drawn in Fig. 5.1. The values of the cross section divided by B(σ) are plotted. The OBTDs which correspond to B(σ) larger than 0.05 (0.1) μ_n^2 in the isoscalar (isovector) excitation are drawn in the figures. Notice that there are good agreements among the distributions at forward angles, 0$-$5°. This indicates that the angular distribution at forward angles are relatively insensitive to details of the wave functions. The insensitivity provides that one angular distribution can be applied to any states for the J^π assignment. The OBTDs which produces the largest B(σ) value is used for comparison with the experimental angular distribution. As another remarkable point, typical shapes of angular distributions are obviously different between the isoscalar and the isovector excitations. The angular distributions of the $T = 0$ excitations are much flatter than those of $T = 1$. It is expected that angular distribution can be used to distinguish the isospin value.

Measured cross sections are compared with the DWBA calculations as shown in Fig. 5.2. The $E_x = 9.50$ MeV state is well known as 1^+, $T = 0$, and the $E_x = 11.45$ MeV

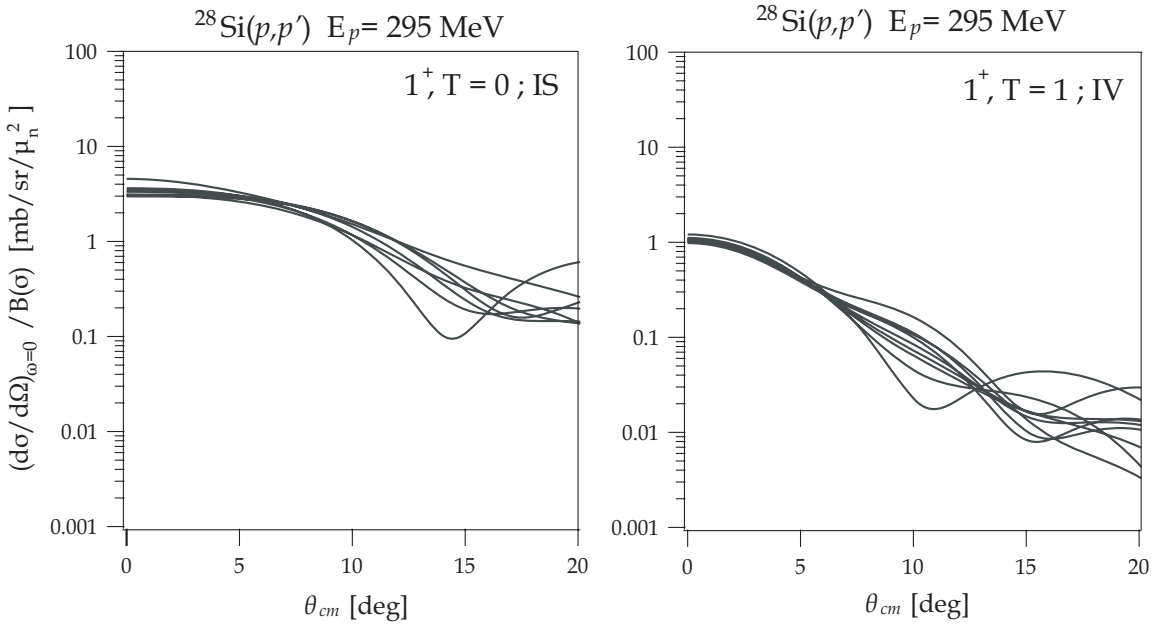

Figure 5.1: Angular distributions calculated by DWBA for various realistic wave functions calculated by using the USD interaction. The values of the cross section divided by B(σ) are potted. All states which are more than B(σ) = 0.05 μ_n^2 in the isoscalar excitation and 0.1 μ_n^2 in the isovector one are drawn. Notice that there are good agreements among the distributions at forward angles, 0−5°.

state as 1^+, $T = 1$. The DWBA curves for both the isoscalar and isovector excitations are drawn in the figures. Normalization factors are applied to the DWBA results for reproducing experiments at forward angles. It is clear that the DWBA slopes at forward angles well reproduce measured angular distributions. We identify the isospin values of other states by using these calculated angular distributions.

5.3.1 1^+, T = 0 (isoscalar) states

The measured angular distributions for the states assigned as 1^+, $T = 0$ are plotted in Fig. 5.3. The 1^+, $T = 0$ angular distribution by the DWBA calculations is also drawn in the figures. We have found three new 1^+, $T = 0$ states at E_x = 13.04, 13.22 (doublet with E_x = 13.19 MeV) and 15.94. For the E_x = 9.50 MeV state, it was accepted that the flatter distribution at $\theta_{cm} = 6-15°$ was due to the contribution from the 2^+ state at E_x = 9.48 MeV [7, 37, 38]. Despite of the present high energy resolution, we almost fail to separate the 2^+ state from the 9.50 MeV one. Although the present angular distribution of the 9.50 MeV state contains some contributions from the 2^+ state, similar trends of the

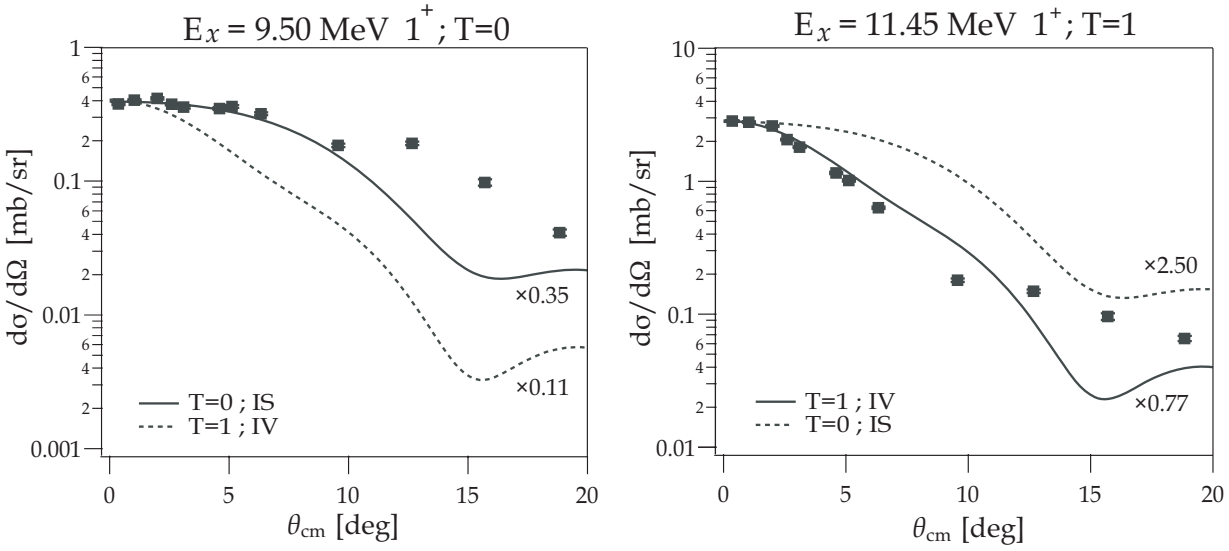

Figure 5.2: Measured (p, p') angular distributions of the E_x = 9.50 MeV (1^+, $T = 0$) and 11.45 MeV (1^+, $T = 1$) state. Normalized DWBA curves are also drawn. It is clear that the DWBA slopes at forward angles reproduce measured angular distributions. The DWBA distributions are used for identification of the isospin value as well as the J^π assignment for other states.

flat slope are seen in other isoscalar ones. It is recognized that the flat distribution at θ_{cm} = 6−15° is common nature of the isoscalar excitation owing to the tensor interaction etc. It implies that the description of the isoscalar excitation mechanism is to be modified in theory.

5.3.2 1^+, T=1 (isovector) states

The measured angular distributions for the state assigned as 1^+, $T = 1$ are plotted in Fig. 5.3. The 1^+, $T = 1$ angular distribution by the DWBA calculations is also drawn in the figures. The DWBA curves well reproduce the experiment results, particularly at forward angles. However, we should pay attention to the 0^+ state which has similar angular distributions to the 1^+ isovector, which is described in Sec. 5.3.3. The present study has found two new 1^+, $T = 1$ states at E_x = 11.95 and 12.24 MeV.

5.3.3 0^+ states

There are several 0^+ states which are similar to 1^+, $T = 1$ with respect to the angular distribution at forward angles. The angular distributions of the 0^+ are plotted in Fig.

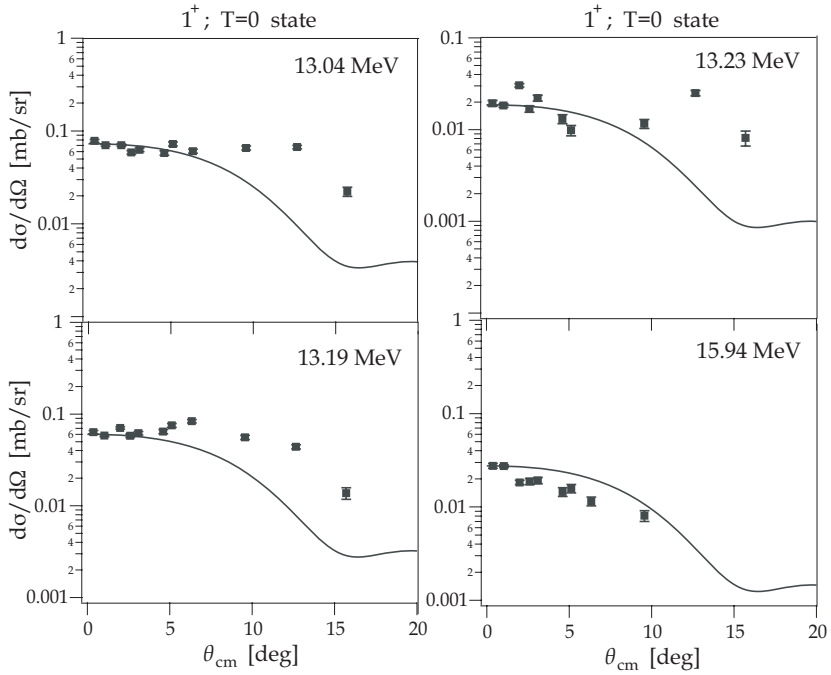

Figure 5.3: Angular distributions for the state identified as 1^+, $T = 0$. Measured (p, p') angular distributions are compared with the normalized 1^+, $T = 0$ DWBA calculations (the solid curves). We have found three new 1^+, $T = 0$ states at $E_x = 13.04$, 13.22 (doublet with $E_x = 13.19$ MeV) and 15.94.

5.5 [B]. The 1^+, $T = 1$ DWBA curves are drawn as the dotted ones in the figure. The measured distributions are steeper than that of 1^+, $T = 1$ curve. It is clear that these states are not 1^+ because the cross sections are largely increasing around $\theta_{cm} = 10{-}20°$. From the similarity to the distribution at $E_p = 201$ MeV shown in Fig. 5.5 [A], they are assigned as 0^+ states. Some of them could be 2^+ state since there are quite differences among the distributions at finite angles. Historically, N. Anantaraman *et al.* [7] assigned to $E_x = 9.72$ and 11.14 MeV states as 0^+. But G.M. Crawley *et al.* [8] gave 1^+, $T = 1$ assignments to the $E_x = 9.72$, 10.80, 11.14, and 12.98 MeV states. Based on the analysis assuming the isospin symmetry, Y. Fujita *et al.* [41] claimed that the $E_x = 9.72$, 11.14, and 12.98 MeV states were the 1^+, $T = 0$ excitations. T. Kawabata [28], however, suggested that the states re-assigned by Fujita have the natural parity, 0^+ or 2^+, from the analysis of polarization transfer observables. The present work supports Anantaraman's and Kawabata's results. Relatively poor energy resolution could have led Fujita to the mis-assignment. Actually, the present study has found a new 1^+, $T = 0$ state at $E_x = 13.04$ MeV, where is very close to 12.98 MeV.

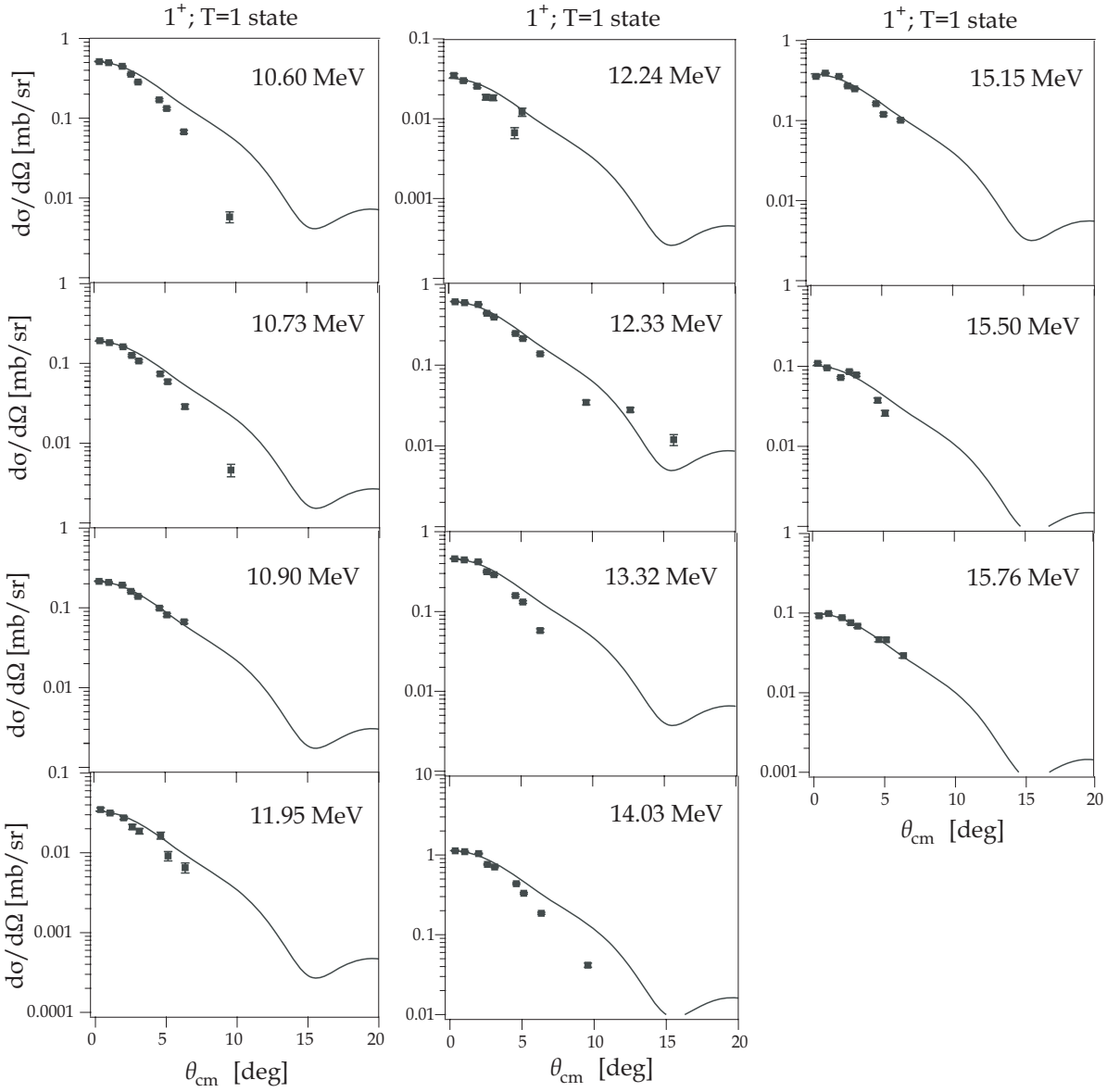

Figure 5.4: Angular distributions for the state identified as 1^+, $T = 1$. Measured (p, p') angular distributions are compared with the normalized 1^+, $T = 1$ DWBA calculations (the solid curves). The present study has found two new 1^+, $T = 1$ states at $E_x = 11.95$ and 12.24 MeV.

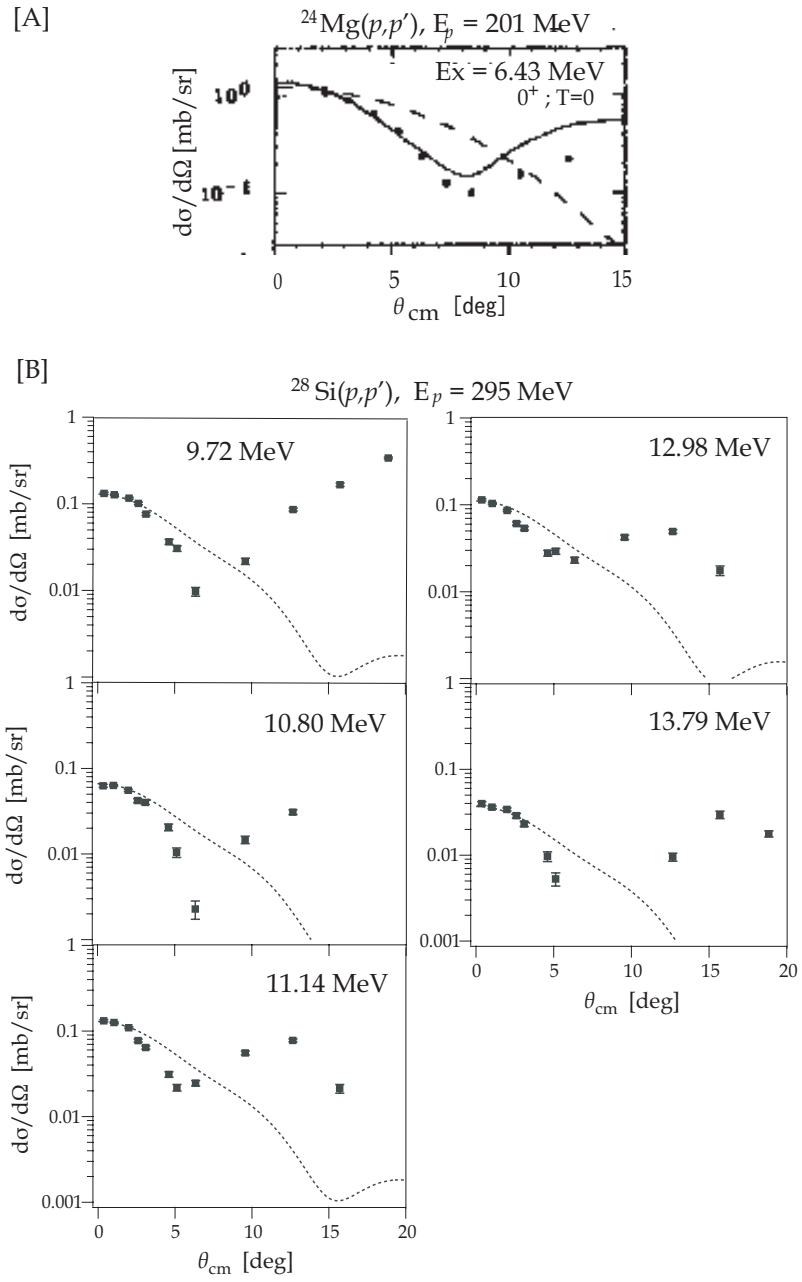

Figure 5.5: Measured angular distributions of 0^+ states. [A] : Figure is taken from Ref. [8]. The solid curve represents the 0^+ distribution by using the code DWUCK [39]. The dashed curve is the 1^+, $T = 1$ distribution by the DWBA. [B] : The present data are compared with the DWBA curve of the 1^+, $T = 1$ excitation. It is clear that these states are not 1^+. They are assigned as the 0^+ states based on the similarity of the angular distribution to that in the panel [A].

5.3.4 Contaminations from other isotopes

Since natural silicon is used as the target, the contaminated states from other isotopes, ^{29}Si and ^{30}Si, could appear in the spectra. Four states corresponding to 1^+ listed in Table 5.1 are excluded from the present study.

Table 5.1: The contaminated 1^+ states from other isotopes [40]. These states are excluded from the present study.

isotope	abundance [%]	E_x [MeV]
^{29}Si	4.7	6.69
		7.05
^{30}Si	3.1	8.95
		9.35

5.4 Unit cross section for B(σ)

5.4.1 Formula of unit cross section

At incident beam energies above 100 MeV/u, one-step direct reaction becomes dominant [42]. The $L = 0$ transfer is enhanced at 0° but the higher multi-pole components ($L > 0$) are suppressed. As mentioned in Ref. [43], the $\Delta L = 0$ cross section at low momentum transfer is expected to be proportional to the strength value. Then, the cross section at 0° in (p, p') reactions $d\sigma/d\Omega|(q, \omega)$ can be related to the corresponding B(σ) value by the following equation

$$\frac{d\sigma}{d\Omega}(q, \omega) = \hat{\sigma}_\sigma F(q, \omega) B(\sigma), \tag{5.1}$$

where $\hat{\sigma}_\sigma$ is a unit cross section for B(σ). The kinematical factor $F(q, \omega)$ is described in Sec. 5.4.2.

5.4.2 Kinematical factor $F(q, \omega)$

The factor $F(q, \omega)$ shows the dependence of the cross section on momentum transfer q and energy transfer ω and is unity at $(q, \omega) = (0, 0)$. This factor is calculated as,

$$F(q, \omega) = \frac{\sigma_{\Delta L=0}(q, \omega)}{\sigma_{\Delta L=0}(0, 0)} \tag{5.2}$$

by using DWBA, where $\sigma_{\Delta L=0}(q,\omega)$ is the cross section. The $F(q,\omega)$ factor is plotted in Fig. 5.6 for both the isoscalar and isovector excitations. When the energy transfer goes to $\omega = 0$, the momentum transfer becomes $q = 0$. In the isoscalar panel, several results for the realistic OBTDs obtained by using OXBASH with the USD interaction are drawn by the solid curves. The arrow in the panel indicates the function used for the kinematical correction which is described in Sec. 5.5.2. This curve is the result for the OBTDs which has the largest B(σ) value. On the other hand, in the isovector panel, just one curve is drawn by the solid line because difference among the results for the obtained OBTDs are very small. The results for various simple $1p1h$ configurations are drawn by the dashed curves except $(1d_{3/2},\ 2s^{-1}_{1/2})$ and $(2s_{1/2},\ 1d^{-1}_{3/2})$ by the dotted curves. The distributions of $1d_{3/2}$-$2s_{1/2}$ configurations in the isovector excitation are quite different from those of other configurations. It is seen that the unique point of the $1d_{3/2}$-$2s_{1/2}$ configurations is a $L = 2$ pairing. Because the realistic distribution in the isovector excitation is very well reproduced by other $1p1h$ configurations, it is understood that the contribution from $1d_{3/2}$-$2s_{1/2}$ configurations is significantly small. The tiny B(σ) strengths which are 10^2-10^3 times smaller than others could be account for a tensor like interactions due to the $L = 2$ nature. In the isoscalar excitations, despite of the small strength by a tensor like interaction, quite difference from other $1p1h$ configurations are not seen although the realistic distributions are different from them. The detail on the $F(q,\omega)$ is not understood.

5.4.3 Obtained unit cross section for B(σ)

In the present study, the unit cross section is obtained from DWBA and OXBASH calculations. The cross section at $(q,\omega) = (0,0)$ divided by the B(σ) value is taken as a unit cross section. The cross section velaues are obtained by DWBA calculations, and the B(σ) values are obtained by shell model calculations using the USD interaction. The relationship between the B(σ) value and the unit cross section is plotted in Fig. 5.7. The averaged value with weighting B(σ) are taken as an obtained unit cross section. There are two reasons for neglecting small strengths. One is that they are quite fluctuating around the average value, and the other is that tiny peaces do not significantly contribute to the

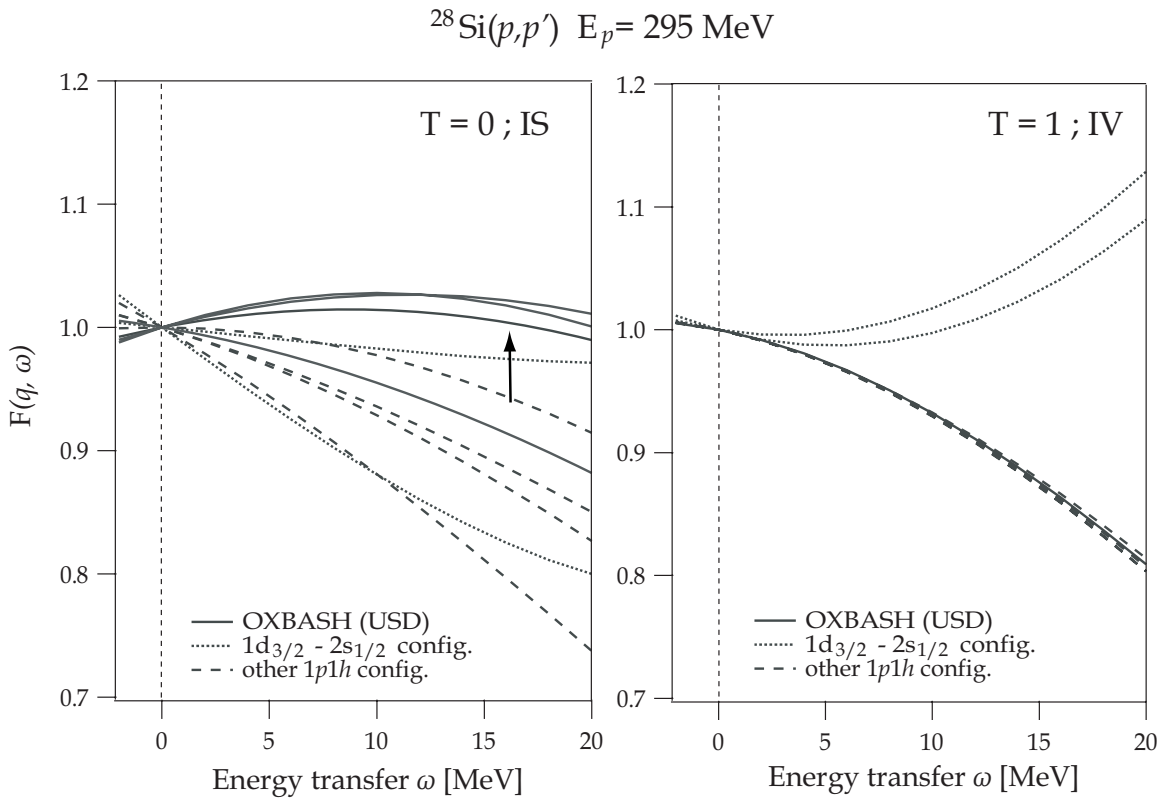

Figure 5.6: Kinematical correction factor $F(q,\omega)$ calculated by DWBA. The solid lines show the result of the realistic configurations obtained by OXBASH using the USD interaction. The arrow in the isoscalar panel indicates the configurations which produce the largest B(σ) values. The dotted lines are the results of simple ($1d_{3/2}$, $2s^{-1}_{1/2}$) and ($2s^{-1}_{1/2}$, $1d_{3/2}$) configurations. The dashed lines are the results for other simple $1p1h$ configurations, $1d_{3/2}$-$1d_{3/2}$, $1d_{3/2}$-$1d_{5/2}$ and $1d_{5/2}$-$1d_{5/2}$.

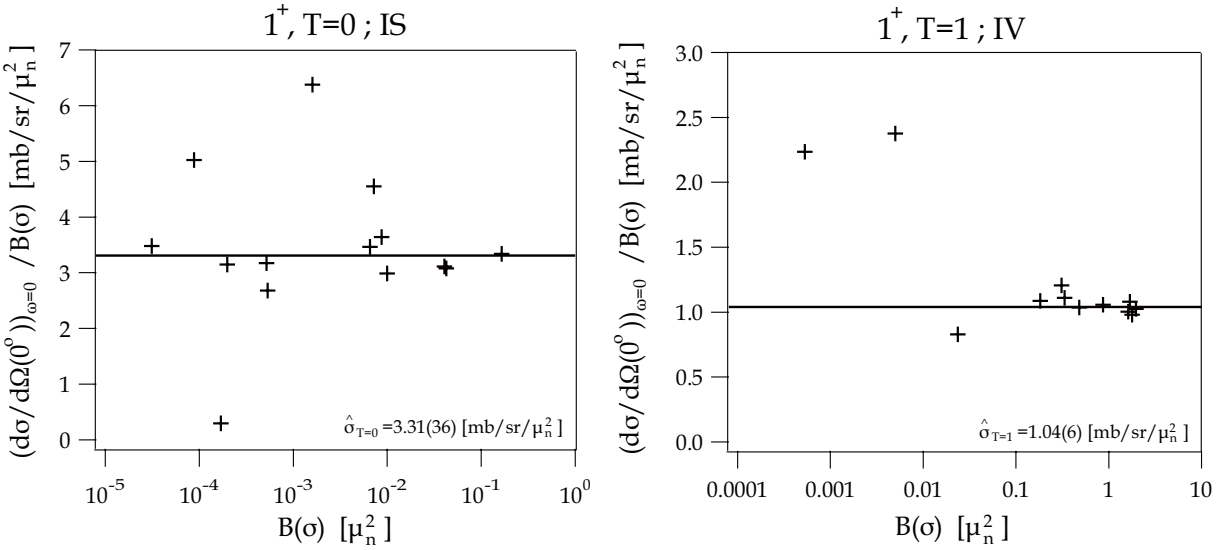

Figure 5.7: The relation between the B(σ) value and the unit cross section obtained by using the DWBA and OXBASH calculations is plotted. The USD interaction is used for OXBASH calculation. The averaged values with weighting B(σ) are taken as an obtained unit cross section, which are drawn in the figures. Since the small strengths are fluctuating around the averaged value, they can be ignored.

total strength. The obtained unit cross sections for both excitations are the followings

$$\hat{\sigma}_{T=0} = 3.31 \pm 0.36 \text{ mb/sr}/\mu_n^2 \tag{5.3}$$

$$\hat{\sigma}_{T=1} = 1.04 \pm 0.06 \text{ mb/sr}/\mu_n^2, \tag{5.4}$$

where $\hat{\sigma}_{T=0}$ and $\hat{\sigma}_{T=1}$ are the unit cross section for the 1^+ isoscalar and the 1^+ isovector excitation, respectively. The uncertainties are from the systematic error owing to ambiguity of wave functions. The choice of the unit cross section is important since it reflects directly on the B(σ) strength. The consistency of the DWBA calculation is studied using ^{12}C data as described in App. A. It is confirmed that the experimental unit cross section is consistent with the calculated one. This confirmation does not promise the consistency of the ^{28}Si unit cross sections, however, it implies that obtained ^{28}Si unit cross sections are relatively correct.

5.5 Conversion to B(σ) strength

5.5.1 Extrapolation to $\theta_{cm} = 0^\circ$

In order to obtain the cross section at small momentum transfer $q \simeq 0$, the measured cross sections are extrapolated to $\theta_{cm} = 0^\circ$. The DWBA curves with the USD interaction are applied to the extrapolations. Since differences in angular distributions due to the wave function are small as seen in Fig. 5.1, typcal curves with of the strongest strength state are used. The energy transfer ω is set to the excitation energy of each state. For the reliable extrapolations, two of the most forward angles data are used, which are measured at $\theta_{cm} = 0.36^\circ$ and 1.03° as described in Sec. 4.1.1. At first, the slopes between these two angle points are determined from the ratio of the DWBA results. The line determined its slope by the calculation is fitted to the observed cross sections with considering the statistical uncertainty. In the fitting, the slope of the line is fixed. Then we obtain the normalization factor for the DWBA curve to reproduce the experiment. The cross section at $\theta_{cm} = 0^\circ$ is taken as the normalized DWBA value at 0°. The ratios of the cross section at 0° to 0.36° are 0.98 ± 0.05 for the isoscalar excitation and 1.00 ± 0.05 for the isovector excitation, where these values are averaged for each state.

5.5.2 Extrapolation to energy transfer $\omega = 0$ MeV

In order to obtain the the cross section at small energy transfer $\omega = 0$ MeV, the cross sections at $(q, \omega) = (q, E_x)$ are extrapolated to the value at $(q, \omega) = (0, 0)$. The realistic $F(q, \omega)$ factor as drawn in Fig. 5.6 is used for the correction. The isoscalar $F(q, \omega)$ factor has $\pm$ 10% uncertainties among wave functions in the energy region of 0$-$15 MeV. The isovector one has small uncertainties among them because tiny contributions from $1d_{3/2}$-$2s_{1/2}$ configurations is negligible.

5.5.3 Obtained B(σ) strength

Since the measured (p, p') cross sections are converted to those at $(q, \omega) = (0, 0)$, the relation between the cross section and B(σ) is expressed by the following equation

$$\left.\frac{d\sigma}{d\Omega}\right|_{q,\omega=0} = \hat{\sigma}_\sigma B(\sigma), \tag{5.5}$$

where $\hat{\sigma}_\sigma$ is $\hat{\sigma}_{T=0}$ or $\hat{\sigma}_{T=1}$. Then, by using the unit cross section obtained in Sec. 5.4, we can deduce B(σ) strength for both the isospin excitations. The measured cross sections at $\theta_{cm} = 0.36°$ and obtained B(σ) strength are summarized in Table 5.2 for isoscalar excitations and in Table 5.3 for isovector ones. The uncertainties of the cross section is statistical error. The uncertainties of the B(σ) strength are from the cross section and the unit cross section errors. Note that the ambiguity from the extrapolation into at $(q, \omega) = (0, 0)$ is not taken into account.

Table 5.2: The measured 1^+ isoscalar cross sections at $\theta_{cm} = 0.36°$ and obtained B(σ) strength. The unit cross section of $\hat{\sigma}_{T=0} = 3.31(36)$ [mb/sr/μ_n^2] is used. See the text for the uncertainty.

E_x [MeV]	$(\frac{d\sigma}{d\Omega})_{0.36°}$ [mb/sr]	B(σ) [μ_n^2]
9.50	0.377 ± 0.008	0.117 ± 0.013
13.04	0.079 ± 0.003	0.022 ± 0.003
13.19	0.064 ± 0.003	0.018 ± 0.002
13.23	0.019 ± 0.001	0.006 ± 0.001
15.94	0.028 ± 0.002	0.008 ± 0.001

Table 5.3: The measured 1^+ isovector cross sections at $\theta_{cm} = 0.36°$ and obtained B(σ) strength. The unit cross section of $\hat{\sigma}_{T=1} = 1.04(6)$ [mb/sr/μ_n^2] is used. In the list, ϕ means not zero but little. See the text for the uncertainty.

E_x [MeV]	$(\frac{d\sigma}{d\Omega})_{0.36°}$ [mb/sr]	B(σ) [μ_n^2]
10.60	0.511 ± 0.010	0.54 ± 0.03
10.73	0.193 ± 0.005	0.20 ± 0.01
10.90	0.215 ± 0.005	0.23 ± 0.01
11.45	2.836 ± 0.043	3.01 ± 0.19
11.95	0.035 ± 0.002	0.04 ± ϕ
12.24	0.035 ± 0.002	0.03 ± ϕ
12.33	0.608 ± 0.011	0.65 ± 0.04
13.32	0.458 ± 0.009	0.49 ± 0.03
14.03	1.124 ± 0.019	1.23 ± 0.08
15.15	0.355 ± 0.008	0.42 ± 0.03
15.50	0.109 ± 0.004	0.11 ± 0.01
15.76	0.093 ± 0.003	0.11 ± 0.01

Chapter 6

Discussion

6.1 Strength fragmentation

The obtained B(σ) strength distributions are shown in Fig. 6.1. The experimental data are drawn in the bottom panel. The results of shell model calculation by using the KUOM and the USD interaction are also shown in the top and the middle panel, respectively. The positions of the strongest strength are well reproduced around $E_x = 9.50$ MeV in the isoscalar excitation and around $E_x = 11.45$ MeV in the isovector one by the shell model calculations. The results of the USD interaction reproduce the experimental data better than those of the KUOM. It is believed that the KUOM interaction does not well reproduce the data of a nuclei which has relatively many valence nucleons. On the other hand, the USD interaction is, within the *sd*-shell, good at reproducing the data of ^{28}Si which has several valence nucleons. Figure 6.1 supports this trend.

In the experimental result, fragmentation of the isovector strength is noticeable compared with that of isoscalar. If the fragmentation is the nature of the isovector excitation, pion behavior in nuclei might be related, which couples to 1^+ ; $(L = 1)$, $T = 0$ state [46]. However, we should also consider a detection limit of the isoscalar strength. The isoscalar $M1$ strength is smaller than the isovector one owing to the destructive interference of the nuclear magnetons [47]. This fact results in the small isoscalar cross section. Since the small cross section is hard to be measured experimentally, few states can be observed. There is still a room to discuss on the fragmentation.

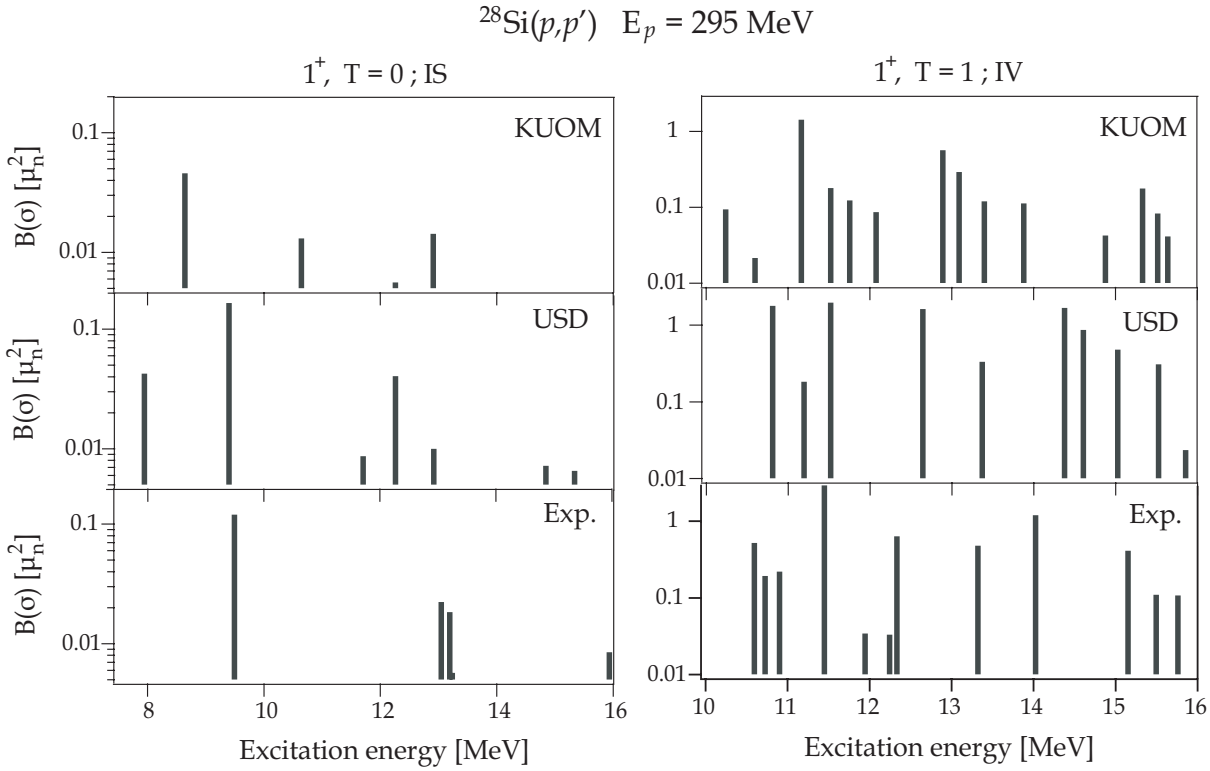

Figure 6.1: Strength distributions of the 1^+, $T = 0$ excitation (left) and the 1^+, $T = 1$ one (right). Top and middle panel shows the results of shell model calculation by using the KUOM and USD interactions, respectively. The present data are shown in the bottom panel.

6.2 Total sum of the strengths

The cumulative sums of B(σ) up to E_x = 16 MeV are shown in Fig. 6.2. The present data are drawn by the solid lines. The shell model calculations using the KUOM (dotted) and the USD (dashed) interactions are compared with the experimental results. The quenching factor R_α is defined as the ratio of experimental to calculated sum, where α is $T = 0$ and $T = 1$. Based on the trend described in Sec. 6.1, the result of the USD interaction is more reliable to discuss on the quenching problem than that of the KUOM. From the results by using the USD interaction, we obtain the quenching factors as

$$R_{T=0} = 0.60 \pm 0.05 \tag{6.1}$$

$$R_{T=1} = 0.76 \pm 0.02, \tag{6.2}$$

where uncertainties are of the statistical and systematic one.

Comparing with the previous work as drawn in Fig. 6.3, $R_{T=0}$ is increased, and $R_{T=1}$ is decreased. It is understood that the present work has found three new isoscalar states and excluded four mis-assigned states for isovector excitations. Here we note that larger uncertainty remains in the determination of isoscalar strength. In fact, the data of isoscalar excitation have not taken so much because of small strengths. Treatments of the tensor force which plays an important role in isoscalar transition bring additional uncertainty. In view of relatively large uncertainty in the isoscalar strength, it is recognized that there are little difference between the isoscalar and the isovector ratios. Then it can be concluded that the Δ-hole admixture has little role in $M1$ quenching of ^{28}Si.

Based on the present study, the $M1$ strength in ^{28}Si is quenched about 70% for both the isoscalar and the isovector excitations. The result of ^{28}Si is consistent with Crawley's result although other *sd*-nucleus were not almost quenched as shown in Fig. 1.1. This can be related to that ^{28}Si is a shell closure nuclei [48]. Systematic study is required in the future.

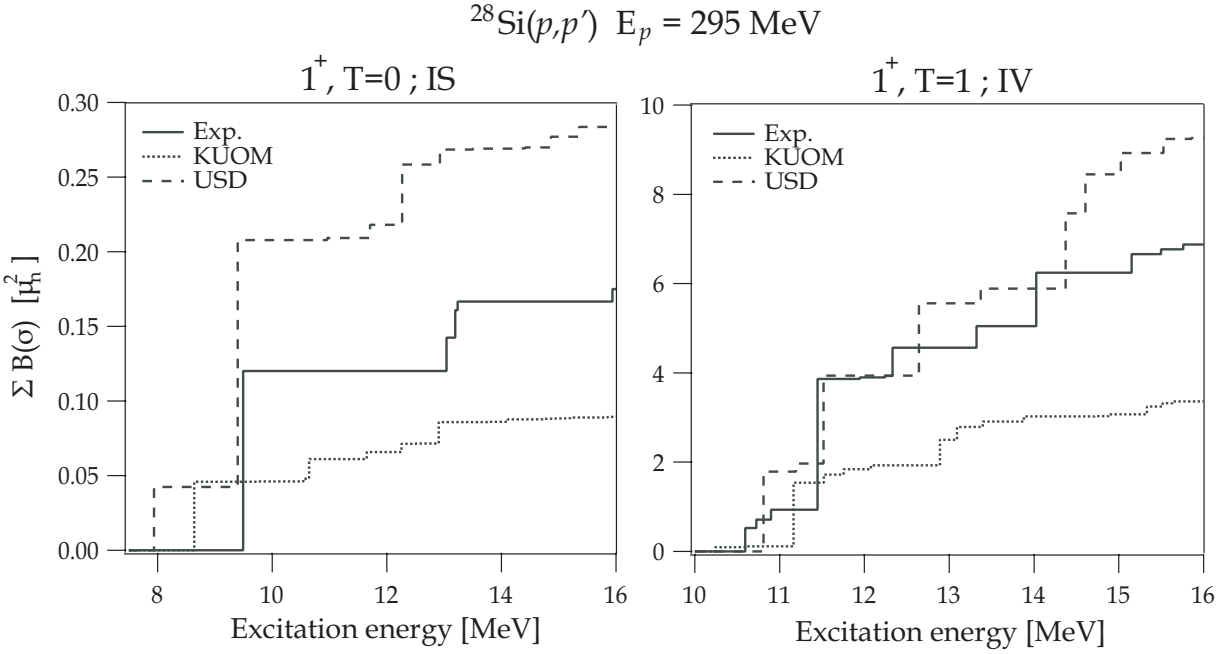

Figure 6.2: Cumulative sums of B(σ) up to E_x = 16 MeV of the 1^+, $T = 0$ strength (left) and the 1^+, $T = 1$ one (right). The present data are drawn as the solid lines. The shell model calculations of the KUOM interaction (dotted) and the USD one (dashed) are compared with the experimental results.

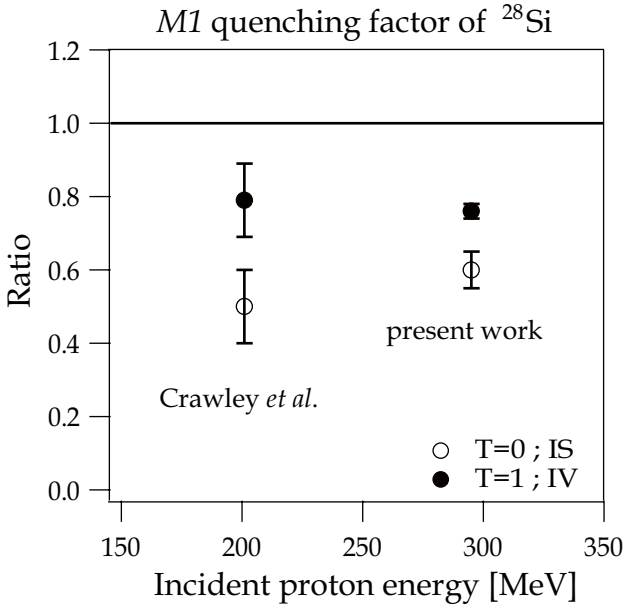

Figure 6.3: Ratios of observed to predicted sums for the isoscalar (opened circle) and the isovector results (filled circle) of the $M1$ strength in ^{28}Si by using (p, p') reactions. The predicted values are obtained by the recent shell model calculations using the USD interaction. The present results are consistent with the previous ones at E_p = 201 MeV [8].

Chapter 7

Conclusion

We have realized the ^{28}Si(p, p') measurements with high resolution at forward angles including zero-degrees at $E_p = 295$ MeV at RCNP. A good scattering angle resolution of $0.5-0.8^\circ$ and a good energy resolution of 20 keV in FWHM have been achieved. Background subtraction has been performed reasonably. By comparing the measured angular distribution with DWBA calculation, the isospin value as well as the spin-parity J^π is assigned. We have found three new 1^+, $T = 0$ states. It can be confirmed that the flatter distribution at $\theta_{cm} = 0-15^\circ$ of the isoscalar excitation is their common nature because similar trends are seen in all 1^+, $T = 0$ distributions. It suggests that the contribution of a tensor force at forward angles should be larger in theory. Two new states which are small strengths are assigned as 1^+, $T = 1$. Four states, which were known as 1^+, $T = 1$, are confirmed that they are not 1^+ but 0^+ or another natural parity states.

The measured cross sections at very forward angles are extrapolated to $\theta_{cm} = 0^\circ$ and to at zero energy transfer, and then they are converted to the B(σ) strength. The unit cross sections obtained by theoretical calculations are used. More fragmentations of the strength can be observed in the isovector excitation than those of the isoscalar excitation. It might be recognized that a pion in nuclei couples to 1^+ ; $(L = 1)$, $T = 0$ state [46]. There is still a room to discuss on the fragmentation. The cumulative sums of B(σ) up to $E_x = 16$ MeV are compared with the shell model calculations using the USD interaction. The ratios of observed to predicted 1^+ sum are less than unity for both the isoscalar and the isovector strengths, which are 60 ± 5 % and 76 ± 2 %, respectively. The strengths quenching of ^{28}Si is consistent with the previous result although those of other *sd*-nucleus were not observed. This can be related to that ^{28}Si is a shell closure nuclei [48]. In view of

relatively large uncertainty in the isoscalar strength, it is recognized that there are little difference between the isoscalar and the isovector ratios. It can be concluded that the Δ-hole admixture has little role in the $M1$ quenching of ^{28}Si.

The present study gives us several pieces of the information on the isoscalar excitations which were not well known. Because we have established almost a perfect measurement for $M1$ strengths by (p, p') reactions, it will be powerful probes to study the nuclear structure.

Appendix A

Unit cross section check of ^{12}C

It is well-known that the DWBA calculations using the Cohen and Kurath interaction [44, 45] well reproduce the cross section data of ^{12}C. This allows us to check the consistency of the DWBA calculation by comparing the calculated unit cross section with the observed one. Parameters input for calculating ^{12}C are the same to those for ^{28}Si except for the effective interaction.

A.1 Deduction of experimental value

The ft value of the β^-decay from the ^{12}B ground state ($g.s.$) to the ^{12}C $g.s.$ is known experimentally as $\log(ft) = 4.066 \pm 0.002$ [49]. We can obtain the B(GT) (Gamow-Teller transition strength) value from experimental ft value by using the following relation [50]

$$\left(\frac{g_A}{g_V}\right)^2 B(GT) = \frac{6145 \pm 4}{ft}, \tag{A.1}$$

where the ratio $(g_A/g_V) = 1.266 \pm 0.004$ [50, 51]. As the schematic figure is shown in Fig. A.1, the obtained B(GT) is analogous to the B(σ) from $g.s.$ to the $E_x = 15.11$ MeV state of ^{12}C. Note that this is on the assumption of the isospin symmetry. Here, B(GT) reduced in isospin is given by [52]

$$B(GT) = \frac{1}{2J_i+1}\frac{1}{2}\frac{C_{GT}^2}{2T_f+1}[M_{GT}(\sigma\tau)^2], \tag{A.2}$$

where C_{GT} is the isospin Clebsch-Gordan (CG) coefficient $(T_iT_{zi}1\pm1|T_fT_{zf})$ with $T_{zf} = T_{zf}\pm1$. In this case, β^- decay, C_{GT} is $(0011|11) = 1$. The matrix element $[M_{GT}(\sigma\tau)]$ denotes the GT transition matrix element of $\sigma\tau$ type. The $M1$ transition strength B($M1$)

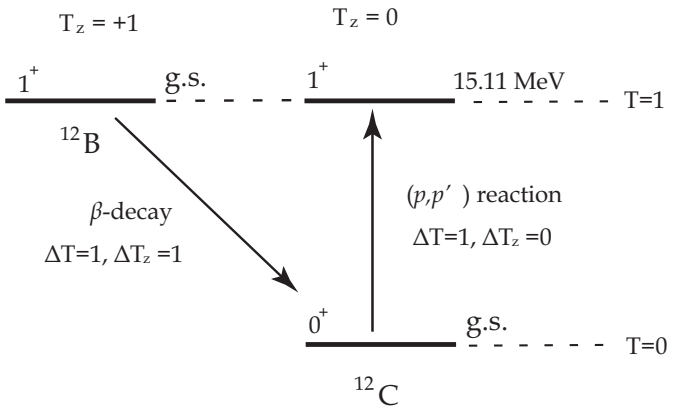

Figure A.1: The schematic figure of isospin analogous transitions in $A = 12$ except for ^{12}N. The Coulomb displacement energies are removed so that the isospin symmetry of the system and that of the transition become clearer. The $M1$ excitation from the ground state to $E_x = 15.11$ MeV in ^{12}C is analogous to the β^-decay from the ground state of ^{12}B.

reduced in isospin is given by [52]

$$B(M1) = \frac{1}{2J_i+1}\frac{3}{4\pi}\mu_N^2\frac{C_{M1}^2}{2T_f+1}\left[g_l^{IV}M_{M1}(l\tau) + g_s^{IV}\frac{1}{2}M_{M1}(\sigma\tau)\right]^2, \tag{A.3}$$

where C_{M1} expresses the isospin CG coefficient $(T_iT_{zi}10|T_fT_{zf})$ with $T_{zf} = T_{zi}$. $M_{M1}(l\tau)$ and $M_{M1}(\sigma\tau)$ are the matrix element of the orbital and spin term, respectively. The bare orbital and spin g factor are g_l^{IV} and g_s^{IV}, respectively. Since we consider (p, p') reactions, only the spin part is probed due to the reaction mechanism. Then Eq. (A.3) is modified to

$$B(\sigma) = \frac{1}{2J_i+1}\frac{3}{4\pi}\mu_N^2\frac{C_{M1}^2}{2T_f+1}\left[g_s^{IV}\frac{1}{2}M_{M1}(\sigma\tau)\right]^2, \tag{A.4}$$

where C_{M1} is $(1010|00) = 1$ and $g_s^{IV} = 4.706$. From the isospin symmetry,

$$M_{GT}(\sigma\tau) = M_{M1}(\sigma\tau) \tag{A.5}$$

is assumed. Using the equations of (A.1), (A.4) and (A.5), we obtain experimental B(σ) value as

$$B(\sigma) = 0.871 \pm 0.003\ \mu_n^2\ \text{mb/sr}. \tag{A.6}$$

Note that the contribution of meson exchange currents (MEC) are neglected because the MEC contribution is generally small in light nuclei.

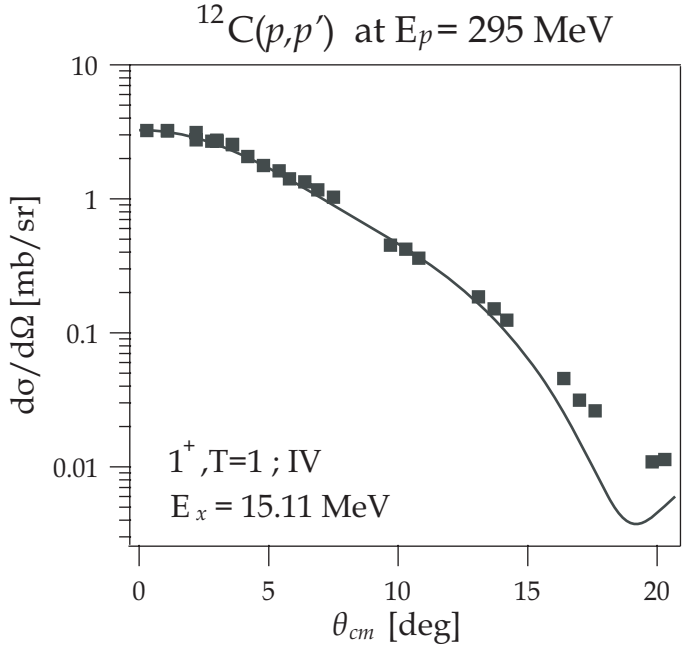

Figure A.2: Angular distribution of $^{12}\mathrm{C}(p,p')$ at $E_p = 295$ MeV. The measured 1^+, $T = 1$ state at $E_x = 15.11$ MeV (square) are compared with a DWBA calculation (line) using the Cohen and Kurath interaction. The experimental values are well reproduced by the calculation.

The $^{12}\mathrm{C}(p,p')$ data are also measured in the present experiment. Similar analysis described in the main chapter are performed and their result is shown in Fig. A.2. The observed unit cross section $\hat{\sigma}_{exp}$ is defined as the following :

$$\left.\frac{d\sigma}{d\Omega}\right|_{q,\omega=0;exp} = \hat{\sigma}_{exp} B(\sigma), \tag{A.7}$$

where $d\sigma/d\Omega|_{q,\omega=0;exp}$ is the experimental cross section value. The measured value at the most forward angle is

$$\left.\frac{d\sigma}{d\Omega}\right|_{\theta_{cm}=0.36°;exp} = 3.24 \pm 0.01 \text{ mb/sr}, \tag{A.8}$$

where uncertainty is of stastical. Then, the cross section is extrapolated to at $(q,\omega) = (0,0)$ and modified to

$$\left.\frac{d\sigma}{d\Omega}\right|_{q,\omega=0;exp} = 3.63 \pm 0.02 \text{ mb/sr}. \tag{A.9}$$

Finally, we obtain

$$\hat{\sigma}_{exp} = 4.17 \pm 0.03 \text{ mb/sr}/\mu_n^2. \tag{A.10}$$

A.2 Consistency check of the unit cross section

The DWBA calculation using the Cohen and Kurath interaction is drawn in Fig. A.2 by the solid line. The obtained unit cross section by the DWBA is

$$\hat{\sigma}_{calc} = 3.54 \text{ mb/sr}/\mu_n^2. \tag{A.11}$$

Here, the values of $B(\sigma) = 0.921\ \mu_n^2$ and $d\sigma/d\Omega = 3.26$ mb/sr are used. The results using other interactions listed in Ref. [44] and [45] fluctuate from the value of Eq. (A.11) within less than one percent. The difference between $\hat{\sigma}_{exp}$ and $\hat{\sigma}_{calc}$ is about 18 percents. Thus, it is confirmed that the DWBA calculation is relatively consistent at least in calculating ^{12}C.

Acknowledgements

本論文を執筆するにあたり、多くの方々のご指導、ご協力を頂きました。

指導教官である民井淳助教授には、M１の入学当初から研究室配属後の実験・解析・執筆までのありとあらゆる場面で適切な指導と助言を頂きました。そして非常にチャレンジングなテーマを頂いたことにも感謝しております。ありがとうございます。また、頭の痛くなるような英文のチェックに付き合わせてしまい申し訳ありませんでした。

畑中教授には高品質のビームを出していただき、おかげで素晴らしいデータが取得できました。藤田佳孝助教授にはゼミに参加させていただき、核構造研究のおもしろさを常に教えていただきました。また研究以外の場面でもお世話になりました。酒見助教授には忙しい中セットアップ、シフトに参加していただき、また常に気を配って頂きました。非常に助かりました。與曽井助教授にも、様々なことでご協力頂きました。LEPS グループに移られてからでも実験中に様子を見に来ていただき、非常に心強かったです。また S.A.S. のオペレーターの皆様に高品質のビームを供給していただいたからこその、本研究であります。感謝しております。

伊藤氏、新原氏、清水氏、藤田訓裕氏、橋本氏にはシフトに参加していただき大変助かりました。特に 2004 年 10 月のビームタイム時では、何もわからない私が多くのことを質問してしまいましたが皆さん快く答えていただきました。本研究の偏極データの解析で、清水氏の修士論文を大いに参考にさせて頂いております。為重氏には、シフト中やまた日常においても最もお世話になっています。とくに二回目のビームタイム時では、二人しかいない深夜シフトにもかかわらずトラブルが続くという日が数夜ありましたが氏のおかげでなんとか対処できました。非常に感謝しております。中西氏には普段の相手のみならず、OXBASH のインストールをしていただき、また使い方も教えていただきました。理研での国際シンポジウムの発表にシェルモデル計算の結果を間に合わせられたのは氏のおかげです。足立氏には南アフリカ滞在において、最もお世話になりました。英語が聞き取れない私は氏に何度も助けられました。また高分解能解析に関する助言も頂きました。

東大ＣＮＳの川畑助手には、実験、解析に関する様々なことに多くの寄与と助言を頂きました。計算コードのメモや助言も非常に有用であり多くの場面で氏に助けられました。感謝しております。ユニットクロスセクションの計算に関して、^{12}Cの実験値でクロスチェックをするというアイデアは氏から頂きました。笹本氏には実験セットアップ、シフトに参加していただきました。人手の少ない時期だったので大変助かりました。

京都大学の坂口助教授、銭広氏にもセットアップ、シフトに参加していただきました。特に坂口助教授の鋭い指摘は、思い込みを考え直すきっかけとなり非常に有意義なものでした。

iThemba LABの藤田浩彦氏には南アフリカ滞在中にお世話になりました。私のようなものでも実験に参加させていただき大変ありがたいです。いい経験になりました。

九州大学の堂園氏にもシフトに参加していただきました。猫の手も借りたい時期であったので非常に助かりました。

I would like to thank Dr. L. Popescu, Prof. B. Rubio and A. Perez for joining the E249 experiment. Talking with them was a good chance for me to improve my English.

一年半、同部屋人として過ごさせて頂いた森信名誉教授には違った視点のアドバイスをよく頂きました。昔の話をよくして下さり、多角的な考え方ができるようになったと思います。

このほか、様々な方々の寄与があって研究を進めて来られました。全員の名前を挙げていませんが、感謝しております。そして最後に後期課程進学を快諾してもらっている両親に感謝したいです。申し訳ありませんが、もうしばらくすねかじりでいさせて頂きます。よろしくお願いします。

平成18年2月　松原礼明

Bibliography

[1] K. Ikeda, S. Fujii and J.I. Fujita, Phys. Lett. **3**, 271 (1963).

[2] C. Gaarde *et al.*, Nucl. Phys. A **369**, 258 (1981), and references therein.

[3] K. Ohta and M. Wakamatsu, Nucl. Phys. A **234**, 445 (1974), and references therein.

[4] A. Arima, in " Spin Excitations in Nuclei", edited by F. Petrovich, G.E. Brown, G.T. Garvey, C.D. Goodman, R.A. Lindgren, and W.G. Love (Plenum, N.Y., 1984), pp.249.

[5] T. Wakasa *et al.*, Phys. Rev. C **55**, 2909 (1997).

[6] K. Yako *et al.*, Phys. Lett. B **615**, 193 (2005).

[7] N. Anantaraman *et al.*, Phys. Rev. Lett. **52**, 1409 (1984).

[8] G.M. Crawley *et al.*, Phys. Rev. C **39**, 311 (1989).

[9] T. Wakasa *et al.*, Nucl. Instr. Meth. A **482**, 79 (2002).

[10] Y. Sakemi *et al.*, Phys. Rev. C **51**, 3162 (1995).

[11] A. Tamii *et al.*, Phys. Lett. B **459**, 61 (1999).

[12] T. Kawabata *et al.*, Phys. Rev. C **65**, 064316 (2002).

[13] Y. Fujita *et al.*, Eur. Phys. J. A **13**, 411 (2002).

[14] H. Fujita, Doctral Dissertation, Osaka Univ, unpublished.

[15] Y. Fujita *et al.*, Nucl. Instr. Meth. B **126**, 274 (1997).

[16] M. Fujiwara *et al.*, Nucl. Instr. Meth. A **422**, 484 (1999).

[17] N. Matsuoka *et al.*, Phys. Lett. B **359**, 39 (1995), and references therein.

[18] P. Ludwig, R. Geller and G. Melin, Review of Scientific Instruments, **63**, p.2892 (1992).

[19] K. Hatanaka *et al.*, Nucl. Instr. Meth. A **384**, 1575 (1997).

[20] T. Noro *et al.*, RCNP Annual Report 1991, p.117.

[21] A. Tamii *et al.*, IEEE Trans. Nucl. Sci. **43**, 2488 (1996).

[22] N. Matsuoka *et al.*, RCNP Annual Report 1991, p.186.

[23] For example, K. Sato *et al.*, to be published in Proc. 17th Int. Conf. on Cyclotrons and Their Applications (Cyclotron 2004); Y. Inata *et al.*, Proc. 4th Workshop on Accelerator Operation, KEK proceedings 2003-19.

[24] H. Fujita *et al.*, Nucl. Instr. Meth. A **469**, 55 (2001).

[25] A. Tamii, Doctral Dissertation, Kyoto Univ. (1999); Private communication.

[26] G.F. Knoll, *Radiation Detection and Measurement*, 3*rd ed*, John Wiley & Sons, Inc., New York (2000).

[27] Web site, http://www.gnu.org/software/gsl/manual/gsl-ref_toc.html

[28] T. Kawabata, Master thesis, Kyoto Univ. (1998), unpublished ; T. Kawabata. *et al.*, RCNP annual report 1997, p.53.

[29] Y. Shimizu, Master thesis, Osaka Univ. (2002), unpublished.

[30] H. Takeda, Memoirs of the Faculty of Science, Kyoto University, Vol. $XXXXIV$. No.1, Article 1, (2003).

[31] K. Lin, Master thesis, Simon Fraser University. (1985), unpublished.

[32] B.A. Brown, Private communication.

[33] For example, B.H. Wildenthal, Prog. Part. Nucl. Phys. **11**, 5 (1984).

[34] T.T.S. Kuo, Nucl. Phys. A **103**, 71 (1967).

[35] J. Raynal, program code DWBA 91, Service de Physique Theorique, CEA-Saclay (1991), unpublished.

[36] M.A. Franey and W.G. Love, Phys. Rev. C **31**, 488 (1985).

[37] O. Häusser *et al.*, Phys. Rev. C **37**, 1119 (1988).

[38] T.N. Taddeucci *et al.*, Phys. Rev. C **43**, 2177 (1991).

[39] P.D. Kunz, program DWUCK, University of Colorado, unpublished.

[40] See web site, http://www.nndc.bnl.gov/nudat2/index.jsp

[41] Y. Fujita *et al.*, Phys. Rev. C **55**, 1137 (1997).

[42] M. Kawai, T. Terasawa and K. Izumo, Nucl. Phys. **59**, 289 (1964).

[43] T.N. Taddeucci *et al.*, Nucl. Phys. A **469**, 125 (1987).

[44] S. Cohen, and D. Kurath, Nucl. Phys. A **73**, 1 (1965).

[45] S. Cohen, and D. Kurath, Nucl. Phys. A **101**, 1 (1967).

[46] H. Toki, Private communication.

[47] For example, F. Osterfeld, Rev. Mod. Phys. **64**, 125 (1987).

[48] Y. Fujita, Private communication.

[49] R.B. Firestone, in *Table of Isotopes*, 1996, edited by V.S. Shirley, published by A Wiley-Interscience Publication.

[50] I. Towner *et al.*, in *Proceedings of the International Conference on the Exotic Nucei and Atomic Masses*, *ENAM*95, Arles, 1995, edited by M. de Saint Simon and O. Sorlin (Detions Frontierer, Gif-sur-Yvette, 1996), p. 711.

[51] K. Schreckenbach *et al.*, Phys. Lett. B **349**, 427 (1995).

[52] Y. Fujita *et al.*, Phys. Rev. C **62**, 044314 (2000), and references therein.